TU Delft

Delft University of Technology

Synthetic thermosphere winds based on CHAMP neutral and plasma density measurements

Gasperini, F.; Forbes, J. M.; Doornbos, E. N.; Bruinsma, S. L.

DOI
10.1002/2016JA022392

Publication date
2016

Document Version
Final published version

Published in
Journal Of Geophysical Research-Space Physics

Citation (APA)
Gasperini, F., Forbes, J. M., Doornbos, E. N., & Bruinsma, S. L. (2016). Synthetic thermosphere winds based on CHAMP neutral and plasma density measurements. *Journal Of Geophysical Research-Space Physics*, *121*(4), 3699-3721. https://doi.org/10.1002/2016JA022392

Important note
To cite this publication, please use the final published version (if applicable).
Please check the document version above.

Copyright
Other than for strictly personal use, it is not permitted to download, forward or distribute the text or part of it, without the consent of the author(s) and/or copyright holder(s), unless the work is under an open content license such as Creative Commons.

Takedown policy
Please contact us and provide details if you believe this document breaches copyrights.
We will remove access to the work immediately and investigate your claim.

This work is downloaded from Delft University of Technology.
For technical reasons the number of authors shown on this cover page is limited to a maximum of 10.

AGU PUBLICATIONS

JGR

Journal of Geophysical Research: Space Physics

RESEARCH ARTICLE

10.1002/2016JA022392

Synthetic thermosphere winds based on CHAMP neutral and plasma density measurements

F. Gasperini[1], J. M. Forbes[1], E. N. Doornbos[2], and S. L. Bruinsma[3]

[1]Department of Aerospace Engineering Sciences, University of Colorado Boulder, Boulder, Colorado, USA, [2]Department of Earth Observation and Space Systems, Delft University of Technology, Delft, Netherlands, [3]Department of Terrestrial and Planetary Geodesy, National Center for Space Studies, Toulouse, France

Key Points:
- CHAMP neutral and electron densities are used to solve the momentum equations for the zonal and meridional winds
- HWM14 is found to largely underestimate the latitude, longitude, and local time variability in the winds
- The zonal and meridional wind longitude structures show large variability with local time and season

Supporting Information:
- Data Set S1
- Data Set S2
- Supporting Information S1
- Figure S1
- Figure S2
- Figure S3
- Figure S4
- Figure S5
- Figure S6
- Figure S7
- Figure S8
- Figure S9
- Figure S10
- Figure S11
- Figure S12
- Figure S13
- Figure S14
- Figure S15
- Figure S16

Correspondence to:
F. Gasperini,
gasperini@colorado.edu

Citation:
Gasperini, F., J. Forbes, E. Doornbos, and S. L. Bruinsma (2016), Synthetic thermosphere winds based on CHAMP neutral and plasma density measurements, *J. Geophys. Res. Space Physics*, *121*, 3699–3721, doi:10.1002/2016JA022392.

Received 21 JAN 2016
Accepted 7 APR 2016
Accepted article online 11 APR 2016
Published online 25 APR 2016

©2016. American Geophysical Union. All Rights Reserved.

Abstract Meridional winds in the thermosphere are key to understanding latitudinal coupling and thermosphere-ionosphere coupling, and yet global measurements of this wind component are scarce. In this work, neutral and electron densities measured by the Challenging Minisatellite Payload (CHAMP) satellite at solar low and geomagnetically quiet conditions are converted to pressure gradient and ion drag forces, which are then used to solve the horizontal momentum equation to estimate low latitude to midlatitude zonal and meridional "synthetic" winds. We validate the method by showing that neutral and electron densities output from National Center for Atmospheric Research (NCAR) Thermosphere Ionosphere Mesosphere Electrodynamics-General Circulation Model (TIME-GCM) can be used to derive solutions to the momentum equations that replicate reasonably well (over 85% of the variance) the winds self-consistently calculated within the TIME-GCM. CHAMP cross-track winds are found to share over 65% of the variance with the synthetic zonal winds, providing further reassurance that this wind product should provide credible results. Comparisons with the Horizontal Wind Model 14 (HWM14) show that the empirical model largely underestimates wind speeds and does not reproduce much of the observed variability. Additionally, in this work we reveal the longitude, latitude, local time, and seasonal variability in the winds; show evidence of ionosphere-thermosphere (IT) coupling, with enhanced postsunset eastward winds due to depleted ion drag; demonstrate superrotation speeds of ~27 m/s at the equator; discuss vertical wave coupling due the diurnal eastward propagating tide with zonal wave number 3 and the semidiurnal eastward propagating tide with zonal wave number 2.

1. Introduction

Wind, temperature, and composition are the fundamental parameters of thermosphere dynamics and structure; from knowledge of composition and temperature one can determine pressure and total mass density using the ideal gas law. In a hypothetical windless atmosphere, temperature, composition, pressure, and density are rather easily related through the hydrostatic law, and this forms the basis for most empirical models of the thermosphere. The addition of winds elevates the complexity of the system considerably, since vertical and horizontal winds modify composition by redistributing chemical species, and can affect temperature through vertical motions (adiabatic heating and cooling). In addition, the bulk wind field responds to changes in pressure as well as collisional momentum transfer with the ionospheric plasma and momentum deposition due to dissipating waves. In particular, the meridional wind component modifies the ionosphere by moving plasma up and down magnetic field lines and serves to transport neutral minor constituents. The meridional wind field can also close with vertical winds on both local and global scales, thus contributing to thermal structure through adiabatic heating and cooling effects. However, the meridional wind field has not been well measured, especially on a global scale.

Thermosphere wind measurements are relatively sparse. Some measurements are possible from the ground using Fabry-Perot interferometers [*Meriwether*, 2006] or incoherent scatter radars [*Salah and Holt*, 1974]. Low-latitude meridional winds at 130–330 km were estimated using ionization gauge data from the Streak mission, but only for the dusk sector [*Clemmons et al.*, 2013]. There have also been some attempts to derive meridional winds through their self-consistency with other observed parameters. Given the proportional relationship between the winds and the height of the F_2 layer peak, magnetic meridional winds can be derived from ionospheric F_2 -layer peak height (h_mF_2) and peak density (N_mF_2) [*Rishbeth*, 1967; *Rishbeth et al.*, 1978].

Thermospheric meridional winds extracted from ionosonde data have been used to investigate diurnal, seasonal, solar cycle and latitudinal variability [*Buonsanto*, 1990, 1991; *Liu et al.*, 2003, 2004], and study changes in the meridional circulation associated with magnetically disturbed conditions [*Forbes et al.*, 1988]. *Luan and Solomon* [2008] derived magnetic meridional winds from h_mF_2/N_mF_2 measurements taken by the Constellation Observing System for Meteorology, Ionosphere, and Climate (COSMIC) satellites, validated this data set using ISR and FPI measurements and found evidence of longitudinal variation of meridional winds induced by magnetic declination effects associated with zonal wind. More recently, *Lomidze et al.* [2015] used the Global Assimilation of Ionospheric Measurements Full Physics (GAIM-FP) model and COSMIC data to infer magnetic meridional winds consistent with observed ionospheric conditions, and *Lomidze and Scherliess* [2015] estimated climatological zonal and meridional winds with the Thermospheric Wind Assimilation Model (TWAM), which combines GAIM-FP magnetic meridional winds with a thermospheric neutral wind model that uses an implicit Kalman filter method.

Some measurements of thermosphere winds were taken as part of the Atmosphere Explorer, Dynamics Explorer, SETA, UARS, C/NOFS missions, but these also provided coarse coverage either due to duty cycle, local time, and latitude restrictions, or limited solar cycle sampling. What we currently know about thermosphere wind behavior is embodied in the Horizontal Wind Model 14 (HWM14) empirical model [*Drob et al.*, 2015], which is a massive multiparameter fit to essentially all of the relevant wind measurements to date. Simultaneous measurements of winds, temperature, and composition are even more rare than wind measurements themselves, yet global simultaneous observations of these fields, and their temporal evolution in response to measured external forcing, are what is really needed to truly understand the physical mechanisms responsible for the dynamics of the thermosphere system.

Despite the somewhat dim perspective laid out above, a remarkable degree of new insights have resulted just from the total mass density measurements derived [*Bruinsma et al.*, 2004; *Doornbos et al.*, 2010; *Doornbos*, 2011] from accelerometer measurements made on the Challenging Minisatellite Payload (CHAMP) and Gravity Recovery and Climate Experiment (GRACE) satellites over the past decade. These span a broad spectrum of topics, including thermosphere variations due to traveling atmospheric disturbances [*Bruinsma and Forbes*, 2010a], the response to solar flares [*Sutton et al.*, 2005] and magnetospheric energy inputs [*Lühr et al.*, 2004; *Liu and Lühr*, 2005], the solar terminator [*Forbes et al.*, 2008; *Liu et al.*, 2009], signatures of plasma-neutral coupling at low latitudes [*Liu et al.*, 2007; *Lühr et al.*, 2007b], the semiannual variation [*Guo et al.*, 2008], solar coronal holes and recurrent geomagnetic activity [*Thayer et al.*, 2008; *Lei et al.*, 2008, 2010], upward propagating solar and lunar tides [*Forbes et al.*, 2009, 2013, 2014], density connections to various solar wind characteristics [*Kwak et al.*, 2009, 2011; *Deng et al.*, 2009; *Knipp et al.*, 2013], and the deep solar minimum of 2008–2009 [*Bruinsma and Forbes*, 2010b; *Lei et al.*, 2011].

The triaxial accelerometer on CHAMP has also enabled some estimate of thermosphere winds in the cross-track direction [*Doornbos et al.*, 2010; *Doornbos*, 2011; *Liu et al.*, 2006; *Häusler et al.*, 2007]. Deriving winds from accelerometer measurements presents a significant challenge. The variations in the in-track accelerations are dominated by neutral density variations. It is therefore not feasible to separately estimate the in-track wind. Because errors in the HWM07-modeled in-track wind are small compared to the orbital velocity, this leads to relatively small errors in the CHAMP densities. At the high altitudes of CHAMP, the cross-track wind determination is highly dependent on the accuracy of the solar radiation pressure model. Radiation pressure modeling errors are the largest when the orbital plane is near dawn-dusk and are minimal for a noon-midnight orbital configuration. Since thermosphere winds are especially large at high latitudes, some success has been achieved in establishing polar region wind patterns and even their dependence on solar wind magnetic field configuration [*Förster et al.*, 2008; *Lühr et al.*, 2007a]. At lower latitudes, with careful data processing and significant averaging, some information on the longitude variability of thermosphere winds has been achieved, including that due to nonmigrating tides propagating upward from the lower atmosphere [*Häusler and Lühr*, 2009; *Lühr et al.*, 2007b; *Liu and Watanabe*, 2008; *Lieberman et al.*, 2013].

In the 1960s and 1970s, before satellite-based wind measurements were made, insights into global patterns of thermosphere wind behavior were obtained by solving the horizontal momentum equations [*Challinor*, 1969; *Geisler*, 1966, 1967], with pressure gradient terms approximated from empirical density and temperature models based on satellite drag [e.g., *Jacchia and Slowey*, 1964; *Jacchia*, 1971] and crude models of the ionosphere and magnetic field geometry. These steady state models mainly showed how ion drag tended to cause cross-isobaric flow in contrast to geostrophic flow and gave some impression about the diurnal behavior

of the wind system, and in some cases its height dependence. Measurements from the CHAMP satellite provide the opportunity to take the above methodology of solving the momentum equations to obtain wind estimates to the next level. In addition to accelerometer measurements of total mass density, a Langmuir probe on CHAMP also provides in situ measurements of electron density. In the present paper we demonstrate how these two measurements can be used to specify the pressure gradient and ion drag terms in the eastward and northward momentum equations of the thermosphere and thus obtain wind estimates (synthetic winds) for the upper thermosphere. Two distinct advantages of this method are that meridional winds can be derived in addition to zonal winds and that these are from a satellite perspective, which can provide different types of insights into the dynamics of the thermosphere than those obtainable from the ground.

The data and models employed in this work are presented in the following section, while the methodology is detailed in section 3. In section 4, we validate the method by showing that neutral and electron densities output from National Center for Atmospheric Research (NCAR) Thermosphere Ionosphere Mesosphere Electrodynamics-General Circulation Model (TIME-GCM) can be used to derive solutions to the momentum equations that replicate reasonably well the winds self-consistently calculated within the TIME-GCM. This provides reassurance that winds computed from the momentum equations with pressure gradients and ion drag coefficients based on observations should provide credible results. Section 5 discusses errors in the derived synthetic winds by implementing the same TIME-GCM simulation used for validation (more details on validation and error analysis are provided in the supporting information S1). In section 6, we reveal the seasonal and local time dependencies of zonal and meridional wind latitude-longitude structures, make comparisons with the empirical HWM14 model and CHAMP cross-track wind, and show examples of new science that can be conducted using this data set.

2. Data

The CHAMP satellite was launched on 15 July 2000 into an almost circular, near-polar (inclination of ~87°) orbit with an initial altitude of 454 km and reentered Earth's atmosphere on 19 September 2010. Due to atmospheric drag the altitude decreased over the 10 year mission life, such that it was around 300 km in 2010 (note that the orbit was raised three times). Given its almost circular, near-polar orbit and to its slow precession (24 h of local time are covered in ~130 days, when considering both the ascending and descending portions of the orbit) CHAMP provided a homogeneous and complete global coverage of the Earth's sphere for atmospheric studies. In this work, we use neutral densities and zonal (cross-track) winds from CHAMP's Spatial Triaxial Accelerometer for Research (STAR) accelerometer [*Bruinsma et al.*, 2004; *Doornbos et al.*, 2010; *Doornbos*, 2011], and electron densities from CHAMP's Digital Ion Drift Meter (DIDM) [*Cooke et al.*, 2003].

As investigated by *Bruinsma et al.* [2004] and *Doornbos* [2011], uncertainty in the drag coefficient and satellite geometry is about 5–15% and is the most important systematic error in neutral density measurements. *Doornbos* [2011] estimated the errors in accelerometer-derived cross-track winds to be mainly caused by uncertainties in the solar radiation pressure acceleration model and by accelerometer calibration biases. Both of these are dependent on the orientation of the orbital plane with respect to the Sun (i.e., solar local time) and on the level of neutral density, such that when densities are low the errors can become as large as a few hundred m/s, and when densities are high (i.e., satellite eclipse and during low solar and geomagnetic activity) the errors are of the order of a few tens of m/s. With respect to the errors in the electron densities (derived from CHAMP Planar Langmuir Probe measurements), *McNamara et al.* [2007] estimated uncertainties up to ~4% at low latitude to midlatitude.

In this study, we also employ numerical modeling simulations to validate the derivation of winds from neutral and electron density measurements. For this purpose, we use the Thermosphere-Ionosphere-Mesosphere-Electrodynamics General Circulation Model (TIME-GCM), the latest in the series of three-dimensional time-dependent developed models by the National Center for Atmospheric Research (NCAR), to simulate the circulation, temperature, electrodynamics, and compositional structure of the upper atmosphere and ionosphere. The NCAR TIME-GCM is a self-consistent time-dependent three-dimensional model from ~30 km in the stratosphere to ~600–750 km (depending on solar cycle) in the upper thermosphere. TIME-GCM solves the fully coupled, nonlinear hydrodynamic, thermodynamic, and continuity equations of the neutral gas together with the ion energy, ion momentum, and ion continuity equations

[*Roble et al.*, 1988; *Richmond et al.*, 1992; *Roble and Ridley*, 1994]. The TIME-GCM predicts global neutral winds, temperature, constituents, electron and ion densities, temperatures and drifts, and the dynamo electric field. Model output with a horizontal resolution of 2.5° × 2.5° and a vertical resolution of 4 points per scale height, with time step of 60 s are used for this study. The amplitudes and phases of the migrating diurnal and semidiurnal tides are specified at the lower boundary using the 2009 Global Scale Wave Model (GSWM-09) [*Zhang et al.*, 2010a, 2010b].

Analyzing the noise in the 10 s resolution CHAMP measured neutral and electron densities and using a 3° latitude bin, we determined that latitude-longitude wind structures can be effectively derived by using 10 day means. For each latitude-longitude bin we determined that averaging ~60 data points (6 measurements per latitude for 10 days) is sufficient to beat down the noise (in part caused by geomagnetic activity effects) and leads to a clean wind product, without compromising the fixed local time assumption (CHAMP precesses 1 h in ~11 days; see section 5 for error estimates). For CHAMP's 10 year lifetime, we identified 115 geomagnetically quiet 10 day periods, defined as the 10 day periods that include a minimum of 8 days with $Ap \leq 10$, and we calculated an average $F_{10.7}$ of 99 solar flux unit (sfu) and standard deviation of 22 sfu for these 115 periods. Defining solar low-condition days with $F_{10.7} \leq 77$, in this paper we restrict our attention to only 63 of these 115 10 day periods that are both at solar minimum and in geomagnetically quiet conditions and span all months at various local times. These prove to be sufficient to study the seasonal and local time variability in the derived winds, as discussed in section 6. We limit our analysis to low- to mid-latitudes (±45°), where the effects of convection electric fields on the neutral dynamics are minimal (in particular at higher latitudes we would expect larger errors in the derivation method due to unmodeled ionosphere-thermosphere coupling effects).

3. Methodology

In this section we describe the methodology used to derive synthetic winds from CHAMP neutral and electron density measurements, including all the assumptions and limitations. The procedure consists of three major steps: (1) deriving temperatures and ion drag values from neutral and electron density measurements, (2) inferring pressure gradients from neutral density measurements, and (3) solving the 2-D momentum equations for the zonal and meridional wind components. Details for each step are provided below.

Step 1 *Deriving temperatures and ion drag values from neutral and electron densities.*

Approach

1. Starting from CHAMP total mass densities derived from accelerometer measurements, we use the Naval Research Laboratory Mass Spectrometer and Incoherent Scatter Radar 00 (NRLMSISE00) empirical model of the thermosphere and iterate on the $F_{10.7}$ solar flux index until the model density converges on the measured density (with a margin of ±1%), yielding the equivalent exosphere temperature from the model. This procedure is possible due to the parametric dependence between exospheric temperature and $F_{10.7}$. The idea of parametrically relating thermosphere densities and temperatures is basic to all empirical models to date, because the vertical distribution of thermosphere density is assumed to follow the barometric law. When temperature is basically independent of height (i.e., for CHAMP at ~300 km) the scale height of each constituent is constant, and a simple exponential dependence with height applies.
2. We infer ion drag coefficients (λ's) from plasma densities measured in situ by CHAMP's Langmuir probe. The Lorentz force, which represents the influence of the ionized plasma on the neutrals, can be expressed as [*Richmond*, 1971]

$$\left[\frac{\vec{J}\times\vec{B}}{\rho}\right]_{\phi} = -\lambda_x(u-u^e) + \lambda_y \cos\theta(v-v^e) \tag{1}$$

for the zonal direction ϕ, and in the latitudinal direction θ as

$$\left[\frac{\vec{J}\times\vec{B}}{\rho}\right]_{\theta} = -\lambda_x(v-v^e) - \lambda_y \cos\theta(u-u^e) \tag{2}$$

where $\vec{J}$ and $\vec{B}$ are the Pedersen current and the magnetic field, respectively, u (v) is neutral zonal (meridional) velocity, u^e (v^e) is zonal (meridional) electrodynamic drift velocity, $\lambda_x = \sigma_1 B^2(\theta)/\rho$, and $\lambda_y = \sigma_2 B(\theta) B_{\text{pole}}/\rho$ are the ion drag coefficients, σ_1 (σ_2) is the Pederson (Hall) conductivity, and ρ is neutral density. If we then

assume that plasma drifts are negligible (see supporting information S1 for the error analysis), and that the masses of ions and neutrals are equal, we can write

$$\lambda_x \approx \frac{N_i}{\rho}\frac{\nu_{ni}}{1+(\nu_{ni}/\omega_i)^2} \tag{3}$$

$$\lambda_y \approx \frac{\nu_{ni}}{\omega_i}\lambda_x \tag{4}$$

where N_i is ion density, ω_i ion gyrofrequency, and ν_{ni} neutral-ion collision frequency, where we then use the approximation $\nu_{ni} = 2.610^{-9}(N/M^{0.5})$ in cgs units [*Chapman*, 1956; *Rishbeth and Garriott*, 1969; *Forbes and Garrett*, 1979].

Step 2 *Deriving pressure gradients from neutral densities and temperatures.*

Approach

1. Pressure (p) is inferred from neutral density (ρ) and temperature (T) derived in Step 1. If we assume ideal gas conditions (very good approximation for the thermosphere, especially under geomagnetic quiet conditions), we can solve the ideal gas law $p = \rho R_{\text{spec}} T$, where R_{spec} is the specific gas constant ($\approx$129.9 J kg^{-1} K^{-1} for atomic oxygen) to derive pressure values.
2. Pressure gradients in the eastward and northward directions are derived by calculating derivatives with respect to longitude ϕ (PGX) and latitude θ (PGY), respectively:

$$\text{PGX} = \frac{1}{R_E \rho \cos\theta}\frac{\partial p}{\partial \phi} \tag{5}$$

$$\text{PGY} = \frac{1}{\rho R_E}\frac{\partial p}{\partial \theta} \tag{6}$$

where R_E is Earth's radius. Note that any longitudinal or latitudinal *mean* biases possibly introduced by the use of MSISE in Step 1 are largely eliminated in the pressure gradients by taking derivatives with respect to longitude and latitude.

Step 3 *Solving the 2-D momentum equations for the horizontal wind field.*

Approach The complete 2-D momentum equations (ignoring vertical velocity effects) in the zonal and meridional directions can be written as [*Dickinson et al.*, 1981]

$$\frac{\partial u}{\partial t} = \frac{\mu}{\rho}\frac{\partial^2 u}{\partial z^2} + f^{\text{cor}} v + \lambda_x(u^e - u) + \lambda_y(v^e - v) - \vec{v}\cdot\vec{\nabla}u + \frac{uv}{R_E}\tan\theta - \frac{1}{R_E\rho\cos\theta}\frac{\partial p}{\partial \phi} - w\frac{\partial u}{\partial z} \tag{7}$$

$$\frac{\partial v}{\partial t} = \frac{\mu}{\rho}\frac{\partial^2 v}{\partial z^2} - f^{\text{cor}} u + \lambda_x(v^e - v) + \lambda_y(u^e - u) - \vec{v}\cdot\vec{\nabla}v + \frac{uu}{R_E}\tan\theta - \frac{1}{R_E\rho}\frac{\partial p}{\partial \theta} - w\frac{\partial v}{\partial z} \tag{8}$$

where u and v are the zonal and meridional velocities, z is height, μ is the viscosity coefficient, f^{cor} is the Coriolis parameter, and u^e (v^e) is the zonal (meridional) plasma drift velocity. Looking at equations (7) and (8), we can say that the time rate of change in the horizontal velocity on the left-hand (first term) side is equal to the forcing terms on the right-hand side. The forcing terms are the following in this order: vertical viscosity (second term), Coriolis force (third term), ion-drag force (fourth and fifth terms), nonlinear horizontal advection (sixth term), curvature momentum force (seventh term), pressure gradient force (eighth term), and vertical advection (ninth term). If we neglect (1) vertical viscosity, (2) plasma drift velocities and parallel ion drag, and (3) nonlinear horizontal and vertical advection and momentum force (second-order terms), and we consider the relationships: $f^{\text{cor}} = 2\Omega\sin\theta$, $\lambda_y = \lambda_x \sin^2 I = \lambda \sin^2 I$ (where I is the magnetic dip angle), where Ω is Earth's rotation rate, we can simplify equations (7) and (8) to the following:

$$\frac{\partial u}{\partial t} = 2\Omega v\sin\theta - \lambda u - \frac{1}{\rho R_E\cos\theta}\frac{\partial p}{\partial \phi} \tag{9}$$

$$\frac{\partial v}{\partial t} = -2\Omega u\sin\theta - \lambda v\sin^2 I - \frac{1}{\rho R_E}\frac{\partial p}{\partial \theta} \tag{10}$$

The left-hand side of the equation (9) (10) shows the time derivative of zonal (meridional) wind with respect to time. The issue is now understanding the relationship between UT time, longitude, and local time in CHAMP's measurements. For each day and for each latitude CHAMP provides a global longitudinal coverage with a resolution of ~24°. Additionally, CHAMP possesses a slow precession rate (24 h of local time are covered in ~260 days) so that we can effectively approximate data for a 10 day period to be at a fixed local time (in reality local time varies by ~4 mins every 24 h). Thus, given CHAMP's precession, we can reformulate (9) and (10) in a latitude versus longitude frame for each 10 day period (*case a*) and in a latitude versus local time frame (at specific longitudes, or as a longitudinal mean) using 130 days of data including both the ascending and the descending nodes (*case b*).

If we consider the linear relationship between universal time (UT) and local time (LT), such that $\delta t_{UT} = \delta t_{LT} - \frac{\delta\phi}{\Omega}$, we can rewrite equations (9) and (10) for case a ($\delta t_{LT} = 0$, so $\delta t_{UT} = -\frac{\delta\phi}{\Omega}$) as

$$\frac{\mathrm{d}u}{\mathrm{d}t_{UT}} = -\Omega\frac{\partial u}{\partial\phi} = -\frac{1}{\rho R_E\cos\theta}\frac{\partial p}{\partial\phi} + 2\Omega v\sin\theta - \lambda u \tag{11}$$

$$\frac{\mathrm{d}v}{\mathrm{d}t_{UT}} = -\Omega\frac{\partial v}{\partial\phi} = -\frac{1}{\rho R_E}\frac{\partial p}{\partial\theta} - 2\Omega u\sin\theta - \lambda v\sin^2 I \tag{12}$$

and for case b ($\delta t_{UT} = 0$, so $\delta t_{LT} = \frac{\delta\phi}{\Omega}$) as

$$\frac{\mathrm{d}u}{\mathrm{d}t_{LT}} = \Omega\frac{\partial u}{\partial\phi} = -\frac{1}{\rho R_E\cos\theta}\frac{\partial p}{\partial\phi} + 2\Omega v\sin\theta - \lambda u \tag{13}$$

$$\frac{\mathrm{d}v}{\mathrm{d}t_{LT}} = \Omega\frac{\partial v}{\partial\phi} = -\frac{1}{\rho R_E}\frac{\partial p}{\partial\theta} - 2\Omega u\sin\theta - \lambda v\sin^2 I \tag{14}$$

Using equation (11) and solving for v as function of u, we can write

$$v = -\frac{1}{2\sin\theta}\frac{\partial u}{\partial\phi} + \frac{1}{2\Omega R_E\rho\sin\theta\cos\theta}\frac{\partial p}{\partial\phi} + \frac{\lambda u}{2\Omega\sin\theta} \tag{15}$$

If we then substitute (15) into (12) we can write

$$\frac{\Omega}{2\sin\theta}\frac{\partial^2 u}{\partial\phi^2} - \frac{1}{R_E\rho\sin(2\theta)}\frac{\partial^2 p}{\partial\phi^2} - \frac{\lambda}{2\sin\theta}\frac{\partial u}{\partial\phi}(1+\sin^2 I) - u\left(2\Omega\sin\theta + \frac{\lambda^2\sin^2 I}{2\Omega\sin\theta}\right) = -\frac{1}{R_E\rho}\frac{\partial p}{\partial\theta} \tag{16}$$

Equation (16) is a second-order partial differential equation for u, of the kind $a\frac{\partial^2 x}{\partial y^2} + b\frac{\partial x}{\partial y} + cx + d = 0$, with a, b , c, and d as known values, in the only variables of longitude and latitude. We solve (16) using the IDL function IMSL-PDE-MOL, which implements the method of lines to represent the solution as cubic Hermite polynomials, and use this calculated value of u to solve for v in equation (12). The same procedure is also applied to solve equations (13) and (14).

Of the three assumptions used to simplify the momentum equations, the more questionable ones are neglecting vertical viscosity and the drift velocities. We neglect vertical viscosity assuming this force to be small compared to pressure gradient and ion drag (as suggested by *Geisler* [1966]); the main role of vertical diffusion is to maintain the horizontal wind field (determined by the pressure gradient and ion drag forces) approximately constant with height. There are some situations where this could be violated; e.g., see section 6.2. We also neglect drift velocities (similar to models such as the Global Scale Wave Model) under the assumption that these have a small effect on the ion drag term at low latitude to midlatitude. For validation and error analyses that bear on these assumptions refer to sections 4 and 5, and supporting information S1.

4. Validation

In order to validate the methodology described in the previous section, we implement TIME-GCM simulations for September at solar minimum ($F_{10.7}$ value of 70 sfu), identical to those analyzed by *Jones et al.* [2013, 2014]. The simulations are static monthly values (i.e., the TIME-GCM is run for 1 day in the middle of the month

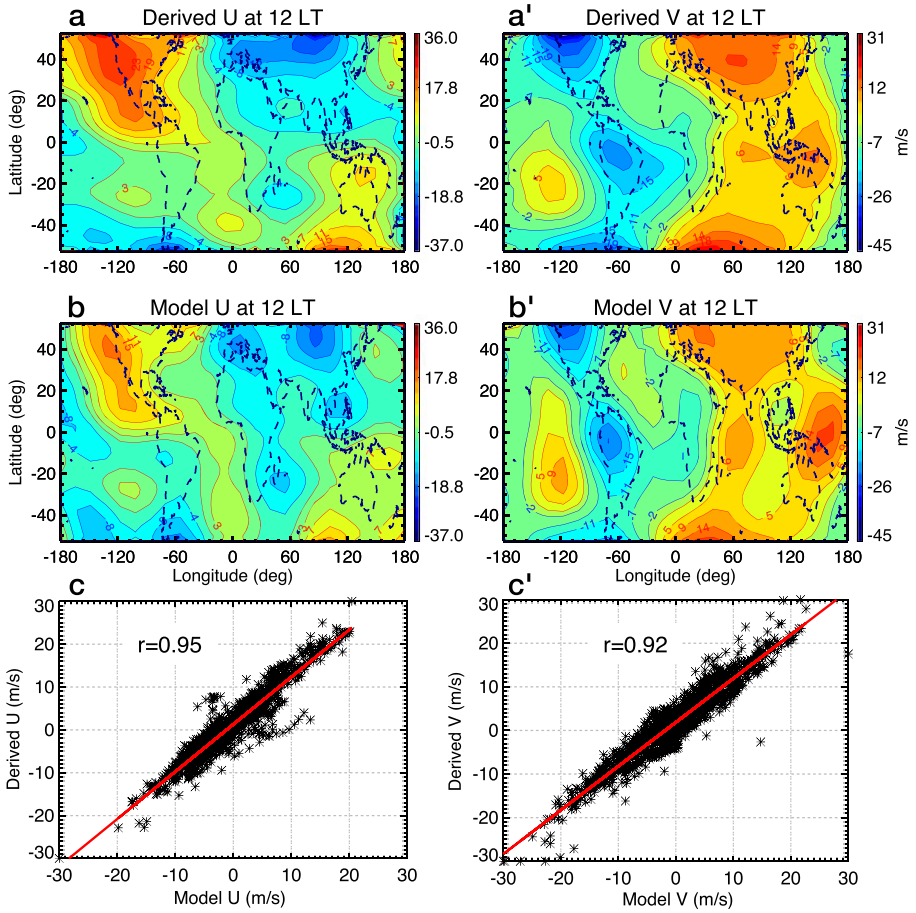

Figure 1. Zonal (a–c) and meridional (a′–c′) latitude-longitude wind structures at 12 LT derived from TIME-GCM neutral and electron densities (Figures 1a and 1a′) and as self-consistently output from the model (Figures 1b and 1b′). A scatter plot between derived and model winds is also included (Figures 1c and 1c′). The model simulation used is for September at solar minimum with tides at the lower boundary. The longitudinal mean was removed to facilitate the comparison. Correlation coefficients of ∼0.95 and ∼0.92 are found for the zonal and meridional winds, respectively.

until the model reaches a diurnally reproducible state) and uses GSWM-09 to specify tidal components at the lower boundary (i.e., 10 mb or 30 km). GSWM-09 includes updated background temperature and wind fields derived from the Sounding of the Atmosphere using Broadband Emission Radiometry (SABER) instrument on TIMED (Thermosphere Ionosphere Mesosphere Energetics Dynamics) satellite measurements, as well as new radiative and latent heating rates derived from the International Satellite Cloud Climatology Project (ISCPP) and Tropical Rainfall Measuring Mission (TRMM) data, respectively [*Zhang et al.*, 2010a, 2010b]. The GSWM-09 boundary includes migrating and nonmigrating diurnal and semidiurnal tidal components with zonal wave numbers ranging between ±6. Supporting information S1 provides additional comparisons for December at solar medium conditions with and without tides at the lower boundary and including and neglecting ion drifts.

Neutral and electron densities from TIME-GCM are converted to pressure gradients and ion drag values, according to the method detailed in section 3 (Step 1 and Step 2), and used to derive solutions to the horizontal momentum equations (Step 3). Figure 1 (2) shows a comparison between the derived (a and a′) and model (b and b′) zonal and meridional winds in a latitude-longitude format for 12 LT (24 LT). A scatter plot between the derived and model zonal and meridional wind components is provided in Figures 1c and 1c′. Comparing Figure 1a (Figure 1b) and Figure 2a (Figure 2b) with Figure 1a′ (Figure 1b′) and Figure 2a′ (Figure 2b′), we can see that the large majority of the longitude-latitude variability in the model winds is effectively replicated by the derived winds. To quantify this, correlation coefficients (*r*'s) are included in the scatter plots. We report correlation coefficients ≥0.92 for both zonal and meridional winds at 12 LT and 24 LT, demonstrating that the derived winds capture ∼85% of the latitude-longitude variability in the model winds.

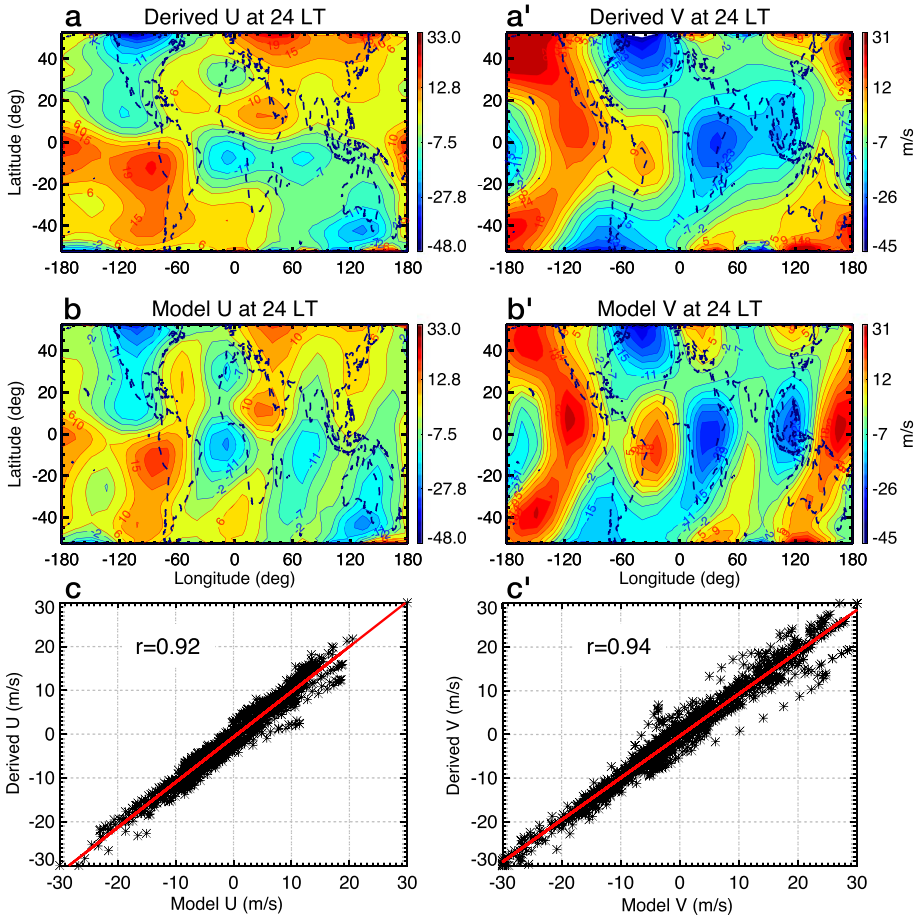

Figure 2. Similar to Figure 1, but for 24 LT. Note correlation coefficients of ~0.92 (~0.94) for the zonal (meridional) wind component.

As discussed in section 3, the horizontal momentum equations can also be solved to reveal the local time variation, when approximating the solution to be UT time independent. To validate this assumption, we implement the same TIME-GCM simulations used to validate latitude-longitude structures. Given the linear relationship between UT time, longitude, and local time (the model runs have a time and longitude resolution of 1 min and 2.5°, respectively), local time is resolvable in the model with a resolution of 1 h. Figure 3 shows the comparison between derived (a and a′) and model (b and b′) zonal and meridional wind structures in a latitude versus local time format as longitude means. Note the strong local time dependence of the longitude-mean winds, with values ranging from 116 m/s to −94 m/s for the zonal component ($\overline{U}$) and 77 m/s to −97 m/s for the meridional component ($\overline{V}$) . To quantify the extent to which the derived winds can reproduce the latitude and local time variability in model winds, a scatter plot between the two is provided in Figures 3c and 3c′, showing $r \approx 0.97$ ($r \approx 0.94$) for zonal (meridional) winds, which translates to a variance of ~94% (~88%). No biases between model and derived winds was found. Similar results (not shown here) are found for different geophysical conditions (i.e., December at solar medium conditions, see supporting information S1) and at specific longitudes, instead of longitude means.

5. Estimated Errors in the Derived Winds

There are three main sources of error that affect the synthetic winds derived from CHAMP measurements. These are (a) errors due to simplifications made in solving the momentum equations, (b) errors in the retrieval of neutral and electron densities from CHAMP accelerometer data, and (c) errors generated by the assumption of constant local time in a 10 day period (only for latitude-longitude structures). The TIME-GCM simulations used to validate the methodology provide the opportunity to estimate the errors due to (a). This is performed for each step in the derivation method outlined in section 3 and for the overall wind estimates. To accomplish

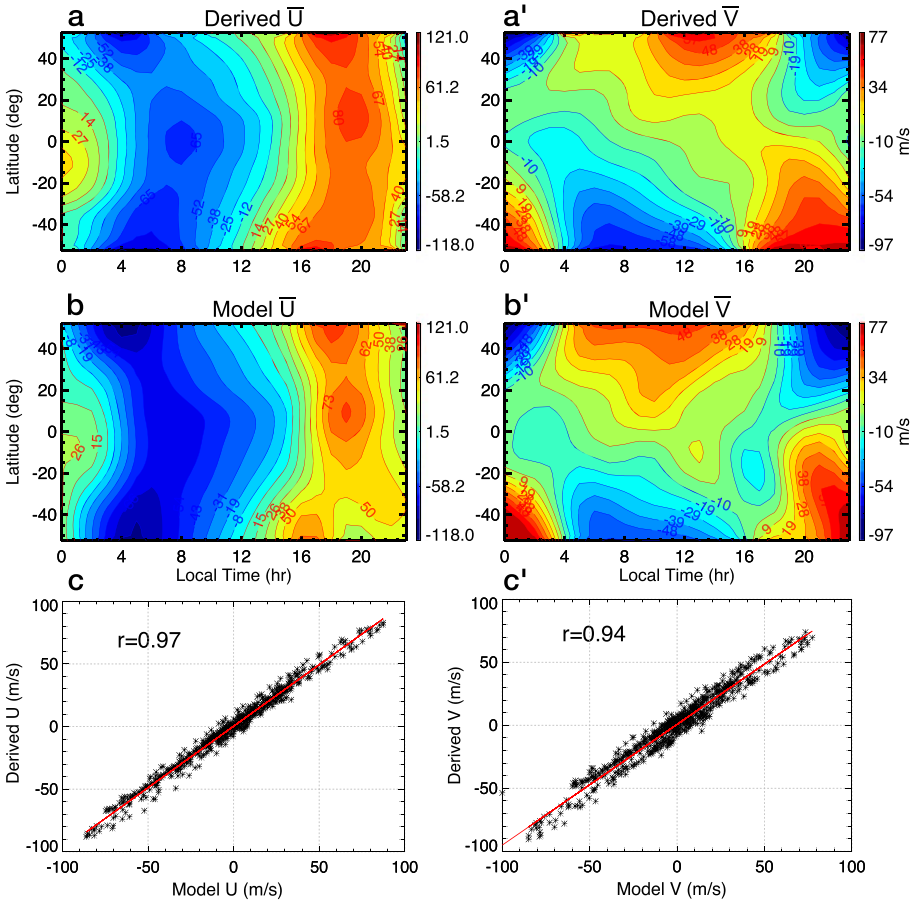

Figure 3. Latitude versus local time comparison between (a) synthetic and (b) model zonal winds (longitudinal mean, $\overline{U}$), and a′ derived and b′ model meridional wind (longitudinal mean, $\overline{V}$). (c (c′)) The scatter plot between synthetic zonal (meridional) winds and model zonal (meridional) winds. The TIME-GCM run used is the same as in Figures 1 and 2. Note correlation coefficients of ~0.97 (~0.94) for zonal (meridional) winds. The minimum in model meridional winds at 10–30°S around 16–18 LT not captured by the derived winds is likely due increased pressure gradient and/or ion drag retrieval errors around sunset for relatively low wind speeds (±15 m/s).

this, we assume the model pressure gradients, ion drag values, and winds as truth, and interpret the differences from the derived pressure gradients, ion drag values, and winds as the errors. For a comprehensive error analysis on the wind derivation method, an interested reader may refer to supporting information S1. Here below we provide a very brief summary of the errors due to (a), (b), and (c).

By performing a scale analysis of the momentum equations, we estimated that neglecting vertical viscosity, horizontal advection, curvature momentum force, and vertical advection in the momentum equations leads to uncertainties of only ~2% in the calculation of the $\frac{du}{dt}$ term. Errors in the derivation of ion drag values from electron densities are estimated to be up to 14%, mainly due to the effect of ion drifts (~12%), while errors in the retrieval of pressure gradients from neutral densities are found to be less than 4% (biases in the MSISE-derived temperatures are largely removed by using longitude-latitude derivatives). Correlation coefficients between the model winds and the winds derived from electron and neutral densities as function of local time and latitude at different local times or as function of local time and latitude at different longitudes (or as longitudinal means) are greater than 0.9 for all the model simulations analyzed. This means that over 80% of the latitude-longitude variability in the zonal and meridional winds can be reproduced by starting from neutral and electron densities alone (as discussed for Figures 1 and 2 in section 4). Errors in the retrieval of neutral and electron densities from CHAMP accelerometer data are also a factor in the overall errors of the derived winds. Errors in the derivation of electron densities from the Planar Langmuir Probe are estimated to be ~4%, while errors in the retrieval of neutral densities from accelerometer measurements are generally less than ~10%. In-track (meridional) winds can impact the quality of the derived neutral densities

Table 1. Local Time and Average Solar Flux Level for Each of the Seven 10 Day Periods Between 1 August and 12 September Selected for the Local Time Reconstruction

Solar Local Time Ascending (Descending) Node	Date (day/month/year)	Average $F_{10.7}$
03 (15)	30/08/07–09/09/07	69
04 (16)	20/08/07–29/08/07	71
10 (22)	04/08/09–13/08/09	68
17 (05)	03/09/08–12/09/08	67
18 (06)	24/08/08–02/09/08	67
19 (07)	12/08/08–22/08/08	67
20 (08)	01/08/08–11/08/08	67

[*Doornbos et al.*, 2010] and cause errors up to ~5% (for meridional winds of ~200 m/s). Additionally, CHAMP local time precession of ~4 min/d yields errors up to 4% in the derived latitude-longitude wind products when assuming fixed local time.

Summarizing, the overall error in the derived winds is estimated to be up to ~30%, although we would expect the real value to be lower due to biases in the derived temperatures being removed by applying derivatives when calculating pressure gradient values, and because we do not expect the total error to be simply the sum of (a), (b), and (c), although this provides a worst case estimate.

6. Results

In this section we first discuss the method adopted to derive the full 24 h local time variability by averaging data for 43 days. Second (section 6.2), we show latitude versus longitude synthetic wind structures at various local times and comparisons with acceleration-derived cross-track winds and HWM14 empirical model winds. Next we analyze the winds in latitude versus local time (section 6.3) and local time versus longitude (section 6.4) formats. In section 6.5 we analyze the latitudinal variability of wave 4, while in section 6.6 we discuss seasonal and local time dependencies in the winds. Note that all data presented in this section refer to low latitude to midlatitude (±45°) and are binned in steps of 3° latitude, 24° longitude, and 1 h local time.

6.1. Local Time Reconstruction

As mentioned in section 2, when analyzing CHAMP's 10 s neutral and electron density measurements, we determined that for a 3° latitude bin averaging 10 days of data is sufficient to beat down the noise, without compromising the fixed local time assumption. Of the 63 geomagnetically quiet 10 day periods that are also at low solar activity, we found 7 to be concentrated within the 43 day period between 1 August and 12 September spanning the years 2007–2009 (see Table 1). Using data from both ascending and descending nodes, and by considering each 10 day period at a fixed local time, for each 3° latitude bin we fit using an equation of the form $A_{n,s}\cos[n\Omega t_{LT}+(s-n)\lambda-\Phi]$, all the waves (diurnal $n=1$, semidiurnal $n=2$, and terdiurnal $n=3$, with zonal wave numbers $s=\pm4$) in the variables of local time (t_{LT}) and longitude (λ), where $A_{n,s}$ is the amplitude of the wave with frequency $n\Omega^{-1}$ and zonal wave number s and Φ is the phase (defined as the time of maximum at zero longitude). Eastward (westward) propagation corresponds to $s<0$ ($s>0$). In the following we refer to this 43 day period, for which all latitudes, longitudes, and local times are adequately sampled to perform the above fit, as an "equivalent day."

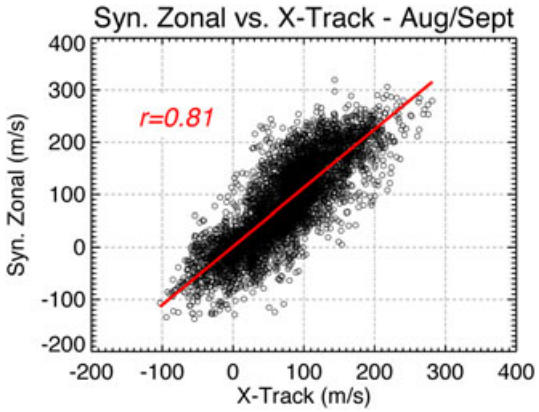

Figure 4. Scatter plot between synthetic zonal winds and cross-track winds for the seven 10 day periods between 1 August and 12 September. For this plot, which includes 3150 data points (14 local times × 15 points in longitude × 15 points in latitude), we report a correlation coefficient of 0.81, which means that the synthetic zonal and cross-track winds share over 65% of the variance. No bias between the two quantities was detected.

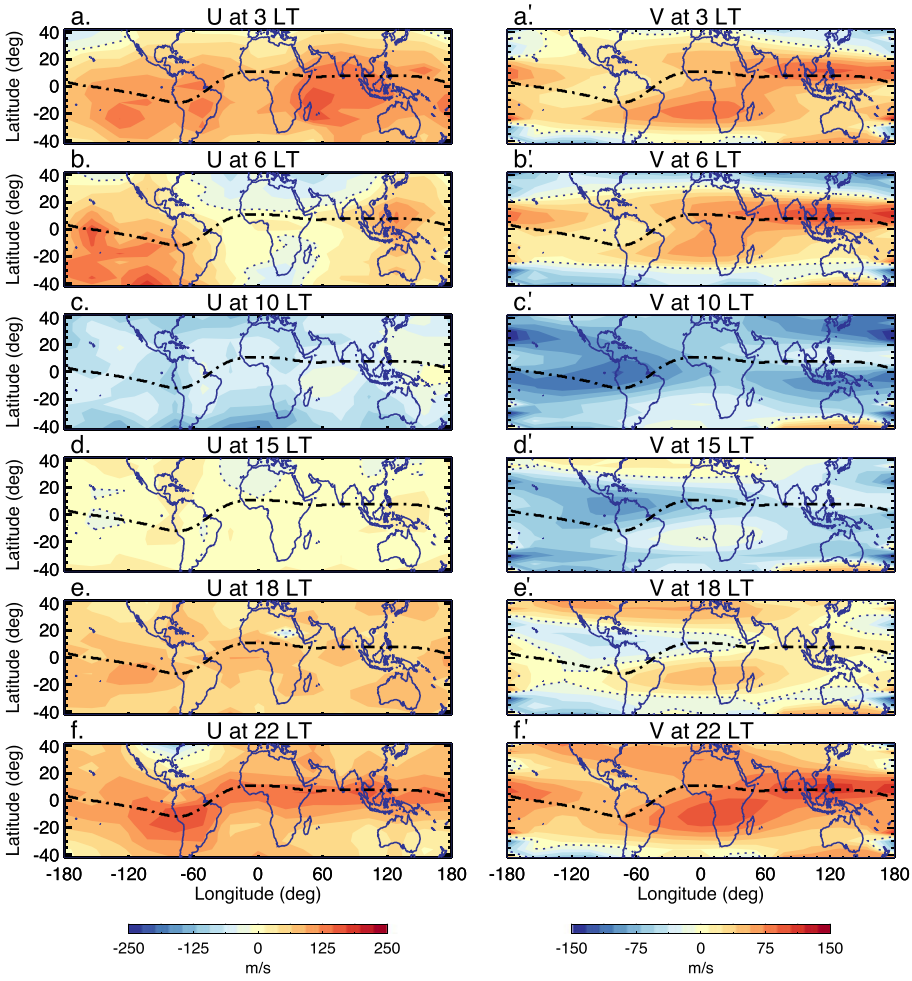

Figure 5. Latitude versus longitude comparisons for synthetic zonal and meridional winds at (a and a′) 3 LT, (b and b′) 6 LT, (c and c′) 10 LT, (d and d′) 15 LT, (e and e′) 18 LT, and (f and f′) 22 LT. The dotted line is the geomagnetic equator. Note the significant local time variability in the latitude-longitude wind structures and the geomagnetic effects in the zonal winds at 22 LT.

The main advantage of averaging data for only 43 days, as opposed to using the ~130 days needed for CHAMP to cover all local times, is an expected amelioration of amplitude suppression due to averaging and possible mixing of seasons (130 days span over 4 months).

In order to compare the synthetic zonal winds with CHAMP accelerometer-derived cross-track winds, we generated a scatter plot between the two wind estimates (Figure 4) that includes data for the 10 day periods listed in Table 1. Figure 4, consisting of 3150 data points (14 local times, 15 longitudes, and 15 latitudes), shows strong correlation between synthetic zonal winds and cross-track winds, with $r \sim 0.81$. This means that the synthetic zonal and cross-track winds share over 65% of the variance in latitude-longitude structures, with no detectable bias between the two quantities. The large number of points and strong correlation further reassures us of the quality of the synthetic wind product derived in this study. More comparisons between cross-track winds and synthetic zonal winds are offered in the following sections.

6.2. Latitude Versus Longitude

A view of the synthetic zonal and meridional winds in a latitude versus longitude format for a variety of local times, chosen on the basis of displaying the range of structures that exist for a 24 h LT period during the equivalent day, is offered in Figure 5. Figure 5 shows significant local time dependency in both zonal and meridional winds. We find eastward zonal winds up to ~200 m/s in the evening (i.e., 22 LT) and westward winds of ~100 m/s around noon (i.e., 10 LT and 15 LT). Low-latitude meridional winds are primarily northward at nighttime (18 LT–6 LT) with speeds up to 75 m/s and become southward around noon

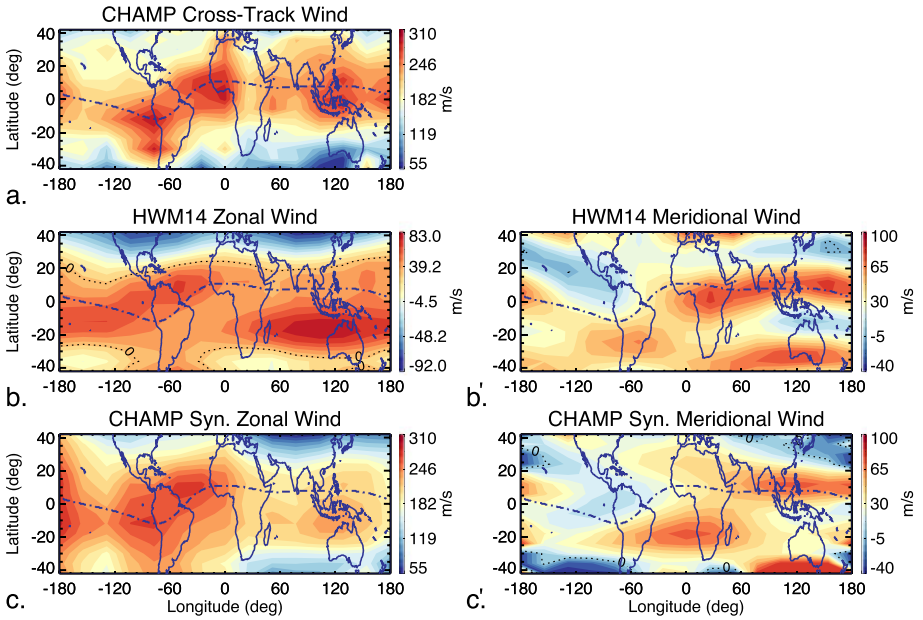

Figure 6. Latitude versus longitude comparisons between (a) CHAMP cross-track wind, (b) HWM14 zonal and (b′) meridional winds, and (c) CHAMP synthetic zonal and (c′) meridional wind for the 10 day period 12–22 August 2008 at 19 LT. The salient features in the synthetic zonal latitude-longitude wind structures compare well with those found in the cross-track winds. The maxima in zonal winds are located around the geomagnetic equator, with speeds up to 250 m/s. Note the poor comparison with HWM14 winds and the different colorbar scale.

(i.e., 10 LT and 15 LT) with speeds of ~50 m/s. This general behavior in wind structures agrees with what is found by *Luan and Solomon* [2008] in winds extracted from COSMIC radio occultation measurements and estimated by the TIME-GCM. From a closer inspection of Figure 5, one can see that at 18 LT (e′) the meridional flow is mainly directed toward the equator for latitudes ±20° and poleward at higher latitudes (particularly evident for longitudes −180° to 60°), which may reflect the effect of the equatorial ionization anomaly (EIA) on the neutral dynamics. As discussed by *Clemmons et al.* [2013], heating associated with EIA crests enhances the neutral pressure, and the resulting pressure gradients drive equatorward and poleward flow away from the pressure maxima. Additionally, from Figure 5 one can see that the zonal (eastward) winds tend to maximize around the geomagnetic equator (dotted black line), in the evening hours (i.e., 22 LT; Figure 5f). This effect is linked to the evening prereversal enhancement of the vertical plasma drift and the uplifting of the *F* region and is discussed below for 19 LT.

Figure 6 presents zonal (cross-track, synthetic, and HWM14) and meridional (synthetic and HWM14) winds in a latitude versus longitude frame at ~19 LT, for post-sunset conditions. Examining Figure 6, we note that (1) synthetic zonal and cross-track winds share the majority of the salient features, with large eastward speeds up to 250 m/s; (2) zonal winds tend to maximize around the geomagnetic equator (black dotted line); and (3) HWM14 zonal winds show similar latitude-longitude patterns, but significantly underestimate the observed speeds.

For (1), we note similar latitude-longitude variability in the synthetic zonal winds (Figure 6c) and cross-track winds (Figure 6a). Eastward winds up to 250 m/s (similar to *Liu et al.* [2006] during September equinox for geomagnetically quiet and solar low conditions) found in the synthetic zonal winds around the geomagnetic equator are also present in the cross-track winds. From a closer examination of Figure 6, one can see sharper gradients (in both latitude and longitude) for cross-track winds than synthetic zonal winds. This is likely due to the effect of smoothing introduced when calculating pressure gradients from neutral densities prior to calculating synthetic winds. Comparing Figures 6c and 6a, one can also see that the synthetic zonal winds in the low-latitude 60° to 180° longitude sector are smaller (by up to 20%) than the cross-track winds. This feature is not present for other local times, suggesting that this is not a systematic error in the synthetic zonal winds but rather a random effect. We also recall that radiation pressure modeling errors in the retrieval of cross-track winds (from accelerometer data) are the largest at dawn-dusk. In addition to larger variances in the cross-track winds, we can also expect greater errors in the derivation of the synthetic winds for dusk conditions.

As discussed in section 5, neglecting vertical viscosity in the derivation of synthetic winds causes errors that are generally smaller than 2%. On the other hand, the reduction in ion drag force at dusk (for more details see the following paragraph) together with the small low-latitude Coriolis force suggests that for this case, vertical viscosity could play a larger role [*Killeen and Roble*, 1984; *Walterscheid and Crowley*, 2015] and be responsible for larger uncertainties in the synthetic winds. *Miyoshi et al.* [2012] investigated the zonal momentum balance in the thermosphere by using an atmosphere-ionosphere coupled model. In Figure 3 of their study, *Miyoshi et al.* [2012] showed that pressure gradient and ion drag play an important role on the zonal momentum budget and that vertical viscosity has a significant effect around the dip equator at dawn and dusk. Thus, some of the differences between the synthetic zonal winds (Figure 6c) and the cross-track winds (Figure 6a) can be explained by larger variances in both cross-track and synthetic winds around dusk.

Regarding (2), Figures 6a and 6c show a clear enhancement in the eastward winds around the geomagnetic equator. This strong low-latitude eastward jet is typical for postsunset hours (i.e., 19 LT) and is due to the combined effect of intensified eastward ion drifts due to vertical electric fields and the rapid increase in height of the ionosphere driven by the evening prereversal enhancement of the vertical plasma drift. Zonal winds in the low-latitude *F* region evening ionosphere generate nearly vertical electric fields (polarization electric fields) that cause the ionospheric plasma to drift in the zonal direction with a velocity approaching that of the neutral wind [*Rishbeth*, 1971; *Miyoshi et al.*, 2012]. This motion of the plasma together with the neutrals drastically reduces the ion drag, which opposes the pressure gradient and acts to limit the wind speed. At low latitudes, where the Coriolis force is small and the balance is mainly obtained between pressure gradient and ion drag, the reduction in ion drag associated with the postsunset uplifting of the *F* layer results in enhanced eastward wind speeds. This phenomenon occurs toward sunset, because this is when the pressure gradient force increases in the eastward direction. *Richmond et al.* [1992] demonstrated that both the uplift of the ionosphere due to the prereversal enhancement [*Anderson and Roble*, 1974] and the small difference between the neutral wind and the plasma drift [*Rishbeth*, 1971] are responsible for the strong eastward wind in the evening. The west-to-east prevailing wind motion of the upper atmosphere, which is both longitude and diurnal mean, is referred to as "superrotation" [*King-Hele*, 1964]. *King-Hele and Walker* [1983] estimated from satellite orbital analysis superrotation speeds of 100 m/s, whereas *Wharton et al.* [1984] found speeds of 20 m/s in Dynamics Explorer (DE) 2 data at high solar flux level, and more recently *Rishbeth* [2002] calculated values of 47 m/s using the TIME-GCM. Using CHAMP data at 400 km, *Liu et al.* [2006] found the superrotation speed to be highly dependent on solar flux level, geomagnetic conditions, and season, with speeds ranging from 10 m/s during solar low and geomagnetic quiet conditions to 60 m/s for solar high and geomagnetically perturbed days. The latitudinal variation of diurnally and longitudinally averaged synthetic zonal winds for the equivalent day is shown in Figure 7. We note the bell-like distribution partly skewed toward the Southern Hemisphere (probably due to the use of geographic instead of geomagnetic coordinates), with maxima around the equator. From Figure 7 we report superrotation speeds of ~27 m/s, significantly larger than the 11 m/s found by *Liu et al.* [2006] for similar geophysical conditions (summer solstice, solar minimum, and geomagnetically quiet conditions). This apparent inconsistency is likely due to the different method used by *Liu et al.* [2006] to derive zonal winds from accelerometer measurements compared to the *Doornbos et al.* [2010] method used in this work. *Liu et al.* [2006] used a direct approach, where the lift and sideways forces are neglected or are modeled and removed from the acceleration beforehand, so that only the observed acceleration due to drag remains. While *Doornbos et al.* [2010] used an iterative approach, where an algorithm is used to make the modeled aerodynamic acceleration match the direction and magnitude of the aerodynamic acceleration observed by the accelerometer. *Doornbos et al.* [2010] reports significant error reduction through the iterative method. Additionally, amplitude suppression caused by the ~130 day averaging performed by *Liu et al.* [2006] could play a role. The superrotation speeds found in this study are in reasonably good agreement with those reported by *Richmond et al.* [1992], *Fuller-Rowell et al.* [1997], and *Rishbeth* [2002] using model simulations.

With respect to (3), note that HWM14 zonal winds (Figure 6b) largely underestimates CHAMP synthetic zonal (Figure 6c) and cross-track (Figure 6a) winds. HWM zonal winds show similar latitude-longitude structures, but with speeds less than ~50% of those observed from CHAMP. This is not surprising considering that HWM wind estimates at 300 km are primarily based on DE2s WATS measurements taken between August 1981 to February 1983 [*Hedin*, 1991]. Since the majority of DE2 measurements were made at solar maximum, the model values are less representative for low solar flux levels, leading to large differences with CHAMP observations [*Liu et al.*, 2006]. Additionally, DE2 orbit was such that it took it one year to cover all local times, hence season and

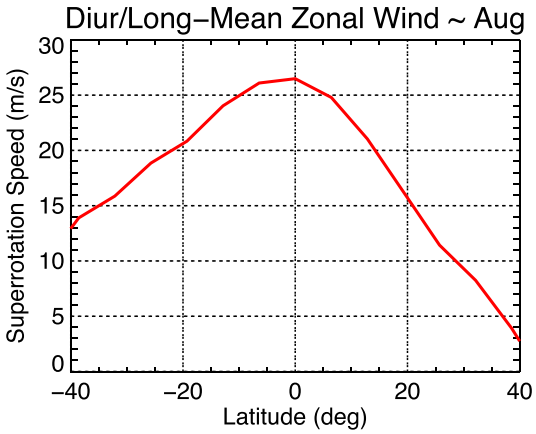

Figure 7. Diurnal and longitude mean zonal winds (superrotation) for the equivalent day as a function of latitude. Note the peak around the equator with maximum of 27 m/s.

local time are locked, with dawn-dusk coverage only in early summer and winter months [*Coley et al.*, 1994]. Thus, since Figure 6 refers to the 10 day period 12-22 August 2008, limited DE2 sampling could explain the model errors. Some of the differences are also likely due to vertically propagating waves measured by CHAMP, but not captured by the empirical model. On the other hand, HWM meridional winds compare well with the synthetic winds both in speed and latitude-longitude structures (Figures 6b′ and 6c′). For more comparisons with HWM and CHAMP cross-track winds see the following sections.

6.3. Latitude Versus Local Time

A different perspective on the winds can be obtained by looking at a latitude versus local time frame. In such a frame one can study the local time variability for a single longitude or as a longitude mean. Figure 8 shows longitudinally averaged ($\overline{U}$ and $\overline{V}$) latitude versus local time structures in synthetic zonal and meridional winds, HWM14, and cross-track winds. Figures 8a and 8a′ show 130 day means (130 days are used to resolve the full 24 h local time variability) for the synthetic zonal and meridional winds, respectively. Figures 8b and 8b′ show zonal and meridional synthetic winds for the equivalent day;

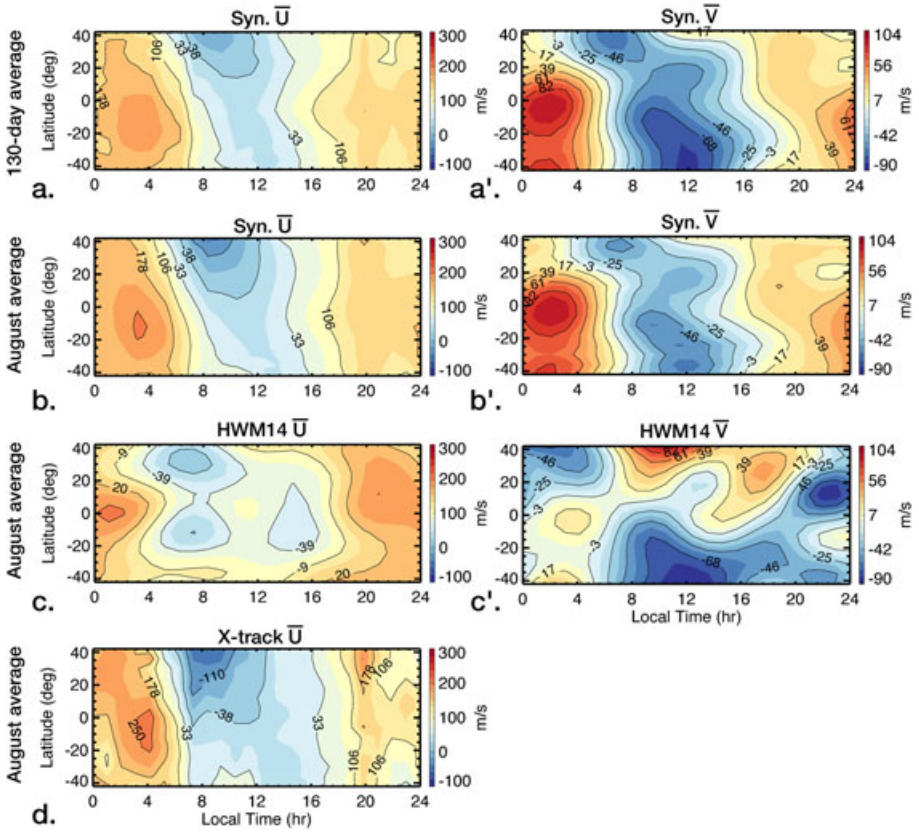

Figure 8. Latitude versus local time plot of (a and b) 130 day mean and ~40 day mean (equivalent day) synthetic (panels a′ and b′) zonal and meridional winds, (c) 40 day mean HWM14 zonal and (c′) meridional winds, and (d) 40 day mean (equivalent day) cross-track winds. Note the many similarities between synthetic zonal and cross-track winds, with HWM14 winds differing significantly from CHAMP winds.

whereas Figures 8c and 8c′ show HWM zonal and meridional winds, and Figure 8d illustrates cross-track winds for the same equivalent day. As discussed in section 6.2, we found large local time variability in both zonal and meridional winds. Eastward winds up to ∼250 m/s and northward winds up to ∼100 m/s are found at nighttime (with maxima at 2 LT). Westward winds up to ∼100 m/s are found around noon (i.e., 10–16 LT), when meridional winds of ∼45 m/s are mainly southward. Figures 8a and 8b) also show the smoothing effect of 130 day averages on the zonal wind, with speeds reduced by up to 30% when compared to the ∼40 day means. On the other hand, Figure 8a′ and 8b′) also show that 130 day average meridional wind has similar speeds to the 40 day averages (or even larger wind speeds for 8–16 LT). Note that any difference between the local time-latitude distribution of cross-track wind presented by *Liu et al.* [2006] and what shown by Figure 8 can be explained by the different method adopted by *Liu et al.* [2006] (direct approach versus iterative approach). Additionally, Figure 8 shows that HWM fails to reproduce most of the observed local time and latitude variability in the winds. Similar conclusions can be drawn for latitude versus local time wind structures at specific longitudes, but these results are not shown here.

6.4. Local Time Versus Longitude

New insights on thermospheric winds can also be acquired by analyzing wind structures in a local time versus longitude frame at a fixed latitude. This frame of reference is preferential to investigate the presence and effect of atmospheric tides. Atmospheric tides are global oscillations of temperature, density, and wind fields induced by the daily cyclic absorption of solar energy in the atmosphere, with periods being subharmonics of one solar day. They can be described as oscillations of the kind: $A_{n,s}\cos(n\Omega t + s\lambda - \phi_{n,s})$. In local time $t_{LT} = t + \lambda/\Omega$, the previous expression becomes: $A_{n,s}\cos(n\Omega t_{LT} + (s - n)\lambda - \phi_{n,s})$. Among the nonsun-synchronous (nonmigrating) tidal components, the eastward propagating diurnal tide with $s = -3$ (DE3) and the eastward propagating semidiurnal tide with $s = -2$ (SE2) are among the largest wave components in the mesosphere/lower thermosphere (MLT). From a sun-synchronous satellite perspective, DE3 and SE2 produce four longitudinal peaks and are the main contributors to the wave 4 structure observed in the ionosphere [i.e., *England et al.*, 2006; *Lin et al.*, 2007; *Pedatella et al.*, 2008] and thermosphere [i.e., *Hagan et al.*, 1997; *Hagan and Forbes*, 2002; *Oberheide et al.*, 2011b; *Gasperini et al.*, 2015].

Figures 9a–9e show a comparison of synthetic, cross-track, and HWM14 winds in a local time versus longitude frame at the equator, again for the 43 day equivalent day. Cross-track and synthetic equatorial zonal winds agree for the majority of the observed longitude and local time variability and show evidence of strong diurnal and semidiurnal components. Both zonal and meridional wind estimates from HWM14 poorly replicate the longitude and local time variability observed in CHAMP. Analyzing the local time versus longitude structures for the equivalent day, we found evidence of a strong wave 4 signal in both zonal and meridional winds (Figures 9a′–9e′). Wave 4 amplitudes of ∼12 m/s (∼14 m/s) in synthetic zonal (cross-track) winds and ∼10 m/s in synthetic meridional winds are found. The local time versus longitude pattern of wave 4 in zonal winds shows clear eastward propagation of ∼90° in 24 h LT, as indicated by the white guiding line. This phase propagation is indicative of the presence of the nonmigrating tide DE3 and thus suggests DE3 to be the cause for the observed wave 4 structure in the zonal wind. Wave 4 in meridional winds propagates ∼120° to the East in 24 h LT and can be explained by the presence of both SE2 and DE3. The following section shows the latitudinal profile of DE3 and SE2 extracted from CHAMP winds, along with comparisons with the Climatological Tidal Model of the Thermosphere (CTMT) [*Oberheide et al.*, 2011a].

6.5. Example of Wave Decomposition

By analyzing local time versus longitude equatorial wind structures for the 43 day equivalent day, we determined wave 4 to be the largest oscillation in zonal winds and among the largest in meridional winds (only surpassed by wave 1), and suggested a link to DE3 and SE2. The presence of a strong wave 4 in the neutral atmosphere is known to impose significant longitudinal variability in the ionosphere, either by modulation of the *E* region dynamo and *F* region fountain [*Sagawa et al.*, 2005; *Immel et al.*, 2006] or by direct penetration into the *F* region [*Forbes et al.*, 2009; *Häusler and Lühr*, 2009; *Oberheide et al.*, 2009, 2011a; *Talaat and Lieberman*, 2010]. Using F_2 layer peak density and the peak height extracted from the COSMIC data set, *He et al.* [2011] found that the generally accepted mechanism of DE3 modulation of *E* region dynamo only accounts for the daytime symmetric components, while the antisymmetric components are likely due to transequatorial neutral winds associated with the SE2 tide. Meridional SE2 winds transport plasma along geomagnetic field lines upward (downward) in the upwind (downwind) hemisphere, thus raising the F_2 layer peak height at the

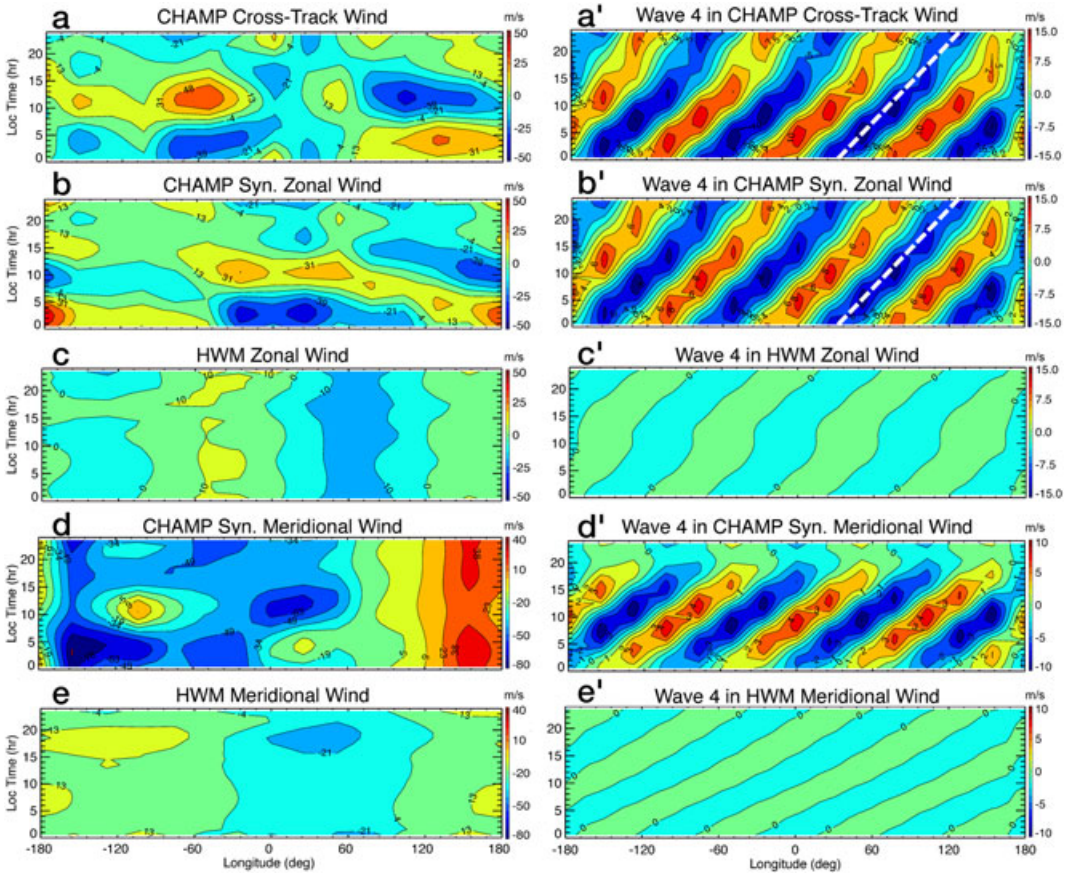

Figure 9. Local time versus longitude structures in (a) cross-track winds, (b) synthetic zonal winds, (c) HWM14 zonal winds, (d) synthetic meridional winds, and (e) HWM14 meridional winds for the equivalent day. (a′–e′) show the wave 4 component of each plot in Figures 9a–9e. The zonal mean was removed from Figures 9a–9e to help the comparison. Note the poor comparison with HWM, which shows very little longitude variability. The white dashed line shows eastward propagation of ~90° in 24 h LT, consistent with DE3.

upwind side and lowering it at the downwind side [*Rishbeth*, 2000], causing ionospheric asymmetry. *Oberheide et al.* [2011b] originally anticipated the role of SE2 meridional winds in producing ionospheric asymmetries about the equator.

Figure 10 shows DE3 and SE2 amplitudes and phases as a function of latitude in synthetic winds (black line), cross-track winds (red), and HWM14 winds (green), retrieved from least squares fitting the local time versus longitude at different latitudes for the 43 day equivalent day. DE3 and SE2 amplitudes in zonal and meridional winds according to CTMT are also plotted (blue line). CTMT is an empirical thermospheric model of upward propagating migrating and nonmigrating diurnal and semidiurnal tides. It provides amplitude and phase for each tidal perturbation from 80 to 400 km and pole-to-pole and is based on Hough Mode Extension (HME, global solutions to the linearized dynamical equations that take into account dissipative effects above the forcing region) fits to TIMED MLT temperatures and winds for the years 2002 to 2008 [*Oberheide et al.*, 2011a]. As shown in Figure 10, we found DE3 maxima of ~12 m/s in equatorial zonal winds and ~8 m/s in meridional winds around 45°S, while SE2 reaches maxima of ~10 m/s in midlatitude zonal winds and ~8 m/s in equatorial meridional winds. These amplitudes of DE3 in the zonal winds (i.e., 12 m/s) are comparable to those found by *Häusler and Lühr* [2009] for August in similar geophysical conditions.

Analyzing Figure 10, one can see similarities between the latitudinal profile of DE3 and SE2 amplitudes and phases in synthetic winds and the amplitudes predicted by CTMT. For the amplitudes, we find one major peak centered around the equator in DE3 zonal winds, two "symmetric" peaks at low latitudes (±45°) in SE2 zonal winds and DE3 meridional winds, and one major peak around the equator and two secondary peaks at higher latitudes (±60°) in SE2 meridional winds. For the phases, DE3 zonal (meridional) winds are mostly symmetric (antisymmetric) about the equator, whereas SE2 zonal winds are mostly antisymmetric and SE2 meridional

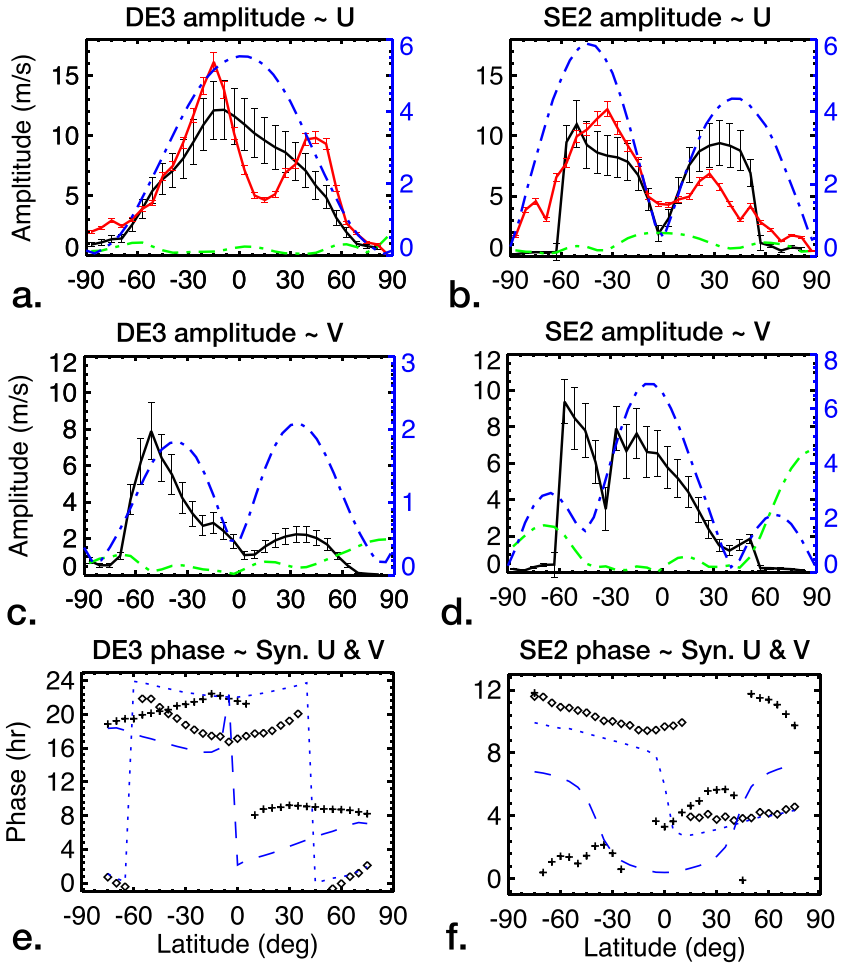

Figure 10. (a and b) Latitudinal profile of DE3 and SE2 in zonal winds for the equivalent day; (c and d) Same as Figures 10a and 10b, but for meridional winds; and (e and f) the latitudinal profile for both zonal and meridional winds of DE3 and SE2, respectively. In Figures 10a–10d, the black line refers to synthetic winds, the red line to cross-track winds, the green line to HWM14 winds, and the blue line shows the amplitude of DE3 and SE2 in CTMT winds for August at 300 km (note the blue *y* axis on the right side of each plot). In Figures 10e and 10f, black crosses (squares) represent synthetic zonal (meridional) wind phases, while the dotted (dashed) blue line shows CTMT zonal (meridional) wind phases. Error bars are included for synthetic and cross-track wind amplitudes, with estimated errors of ~20% and ~5%, respectively. Note the small amplitudes in HWM14 and significant departure of DE3 and SE2 latitudinal structures from that of CTMT.

winds have a more complex latitudinal structure. More interestingly though, we also find large differences between SE2 and DE3 in CHAMP winds and those predicted by CTMT. First, the amplitudes of DE3 and SE2 in CTMT winds are ~50–70% smaller than the ones found in CHAMP (note the different *y* axis for CTMT); this effect is likely due to amplitude suppression caused by CTMT's multiyear averaging. Second, the latitudinal shape of observed DE3 and SE2 is significantly different from that of CTMT. To understand the cause of this difference, we need to consider that CTMT tidal predictions at 300 km are based on the vertical extrapolation of HMEs, and neglects any tide-mean flow interactions (or nonlinear wave-wave interactions). As shown in Figure 10a, DE3 in zonal winds is dominated by its hemispherically symmetric mode, consistent with what is found by *Truskowski et al.* [2014] at the base of the thermosphere (110 km). DE3 is known to be generated in the tropical troposphere by latent heat release, and its first symmetric mode (which is a Kelvin wave) has been shown to propagate high into the thermosphere due to its vertical wavelength of ~56 km [*Oberheide et al.*, 2011a]. A careful analysis of Figure 10a also reveals the presence of a nonnegligible antisymmetric component of DE3 zonal winds (the amplitudes are partly skewed toward the Southern Hemisphere). Looking at Figure 10c, we find DE3 in meridional winds to be not purely antisymmetric (as predicted by HMEs, and shown by CTMT), but significantly skewed toward the Southern Hemisphere (similarly to DE3 in zonal winds

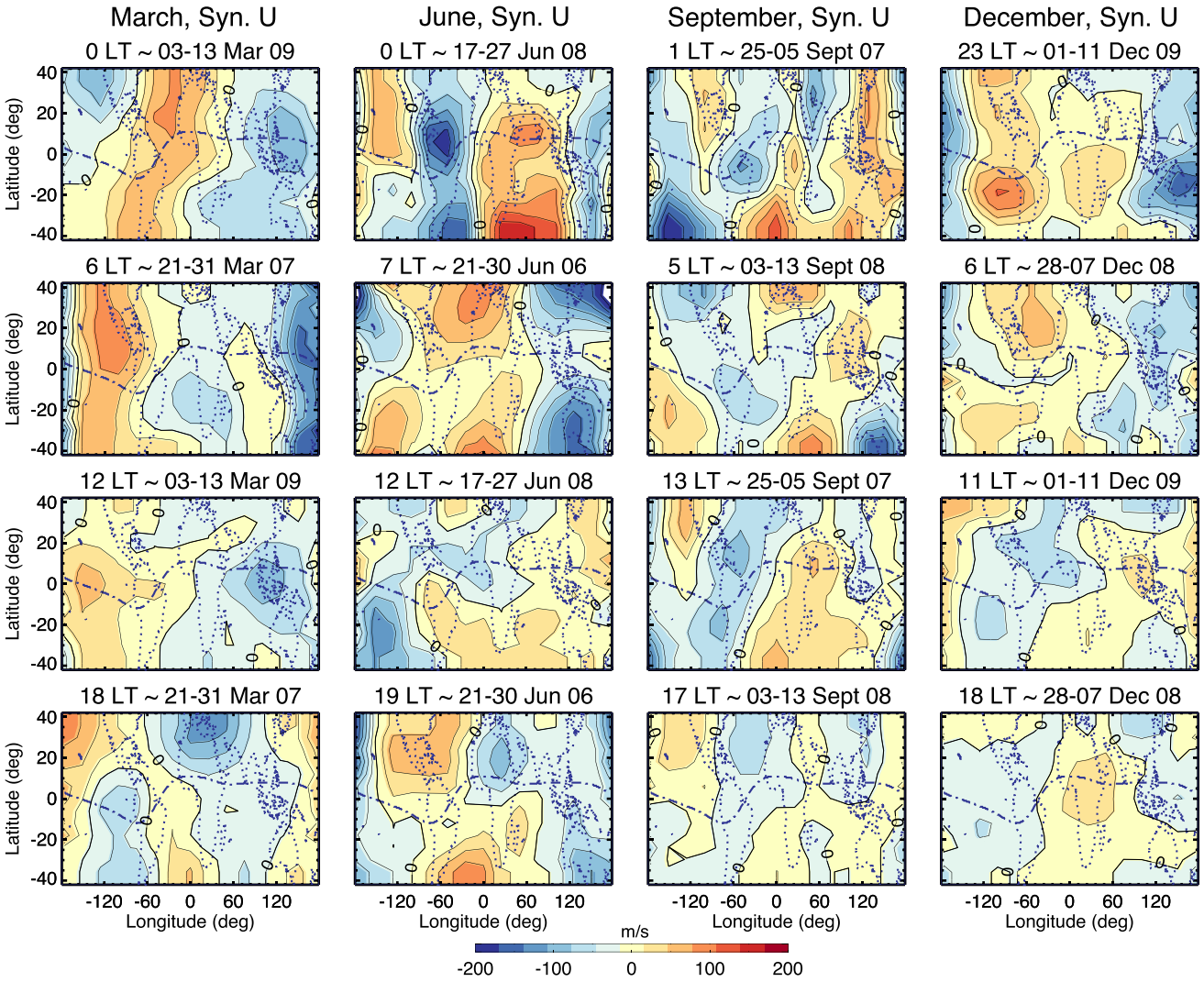

Figure 11. Latitude-longitude structures in the synthetic zonal wind for the months of March, June, September, and December around noon (i.e., 12 LT), midnight (i.e., 0 LT), dawn (i.e., 6 LT), and dusk (i.e., 18 LT). Note the strong seasonal and local time variability in the winds and the significant presence of wave 2, wave 3, and wave 4.

and SE2 in meridional winds). One possible explanation for the presence of this antisymmetric component is given by mode coupling, wherein a given mode (i.e., symmetric mode) interacts with the mean flow to contribute to the generation of other modes (e.g., antisymmetric modes). Despite mode coupling, individual modes tend to retain their properties in terms of vertical propagation [*Lindzen et al.*, 1977]. The first antisymmetric mode of DE3 has a vertical wavelength of ~30 km [*Truskowski et al.*, 2014] and does not propagate to CHAMP heights. Thus, if DE3 is symmetric at ~100 km, then its distortion is due to mode coupling occurring between ~100 km and ~300 km. We know that for eastward propagating waves (such as DE3 and SE2), the frequency is Doppler-shifted to higher absolute values in regions of westward wind and to lower absolute values in regions of eastward wind. In regions where dissipation is important, waves with large Doppler-shifted frequency are less effectively damped than those with smaller Doppler-shifted frequency; thus, a wave exhibits larger amplitudes if Doppler-shifted to higher absolute frequencies. With this in mind, our results would indicate the presence of stronger eastward winds in the Northern Hemisphere, or westward winds in the Southern Hemisphere, in the ~100–300 km height region. The situation is more complicated for SE2, which can be generated in situ by nonlinear interactions between DE3 and DW1 [*Oberheide et al.*, 2011a], in addition to propagating upward from lower altitudes.

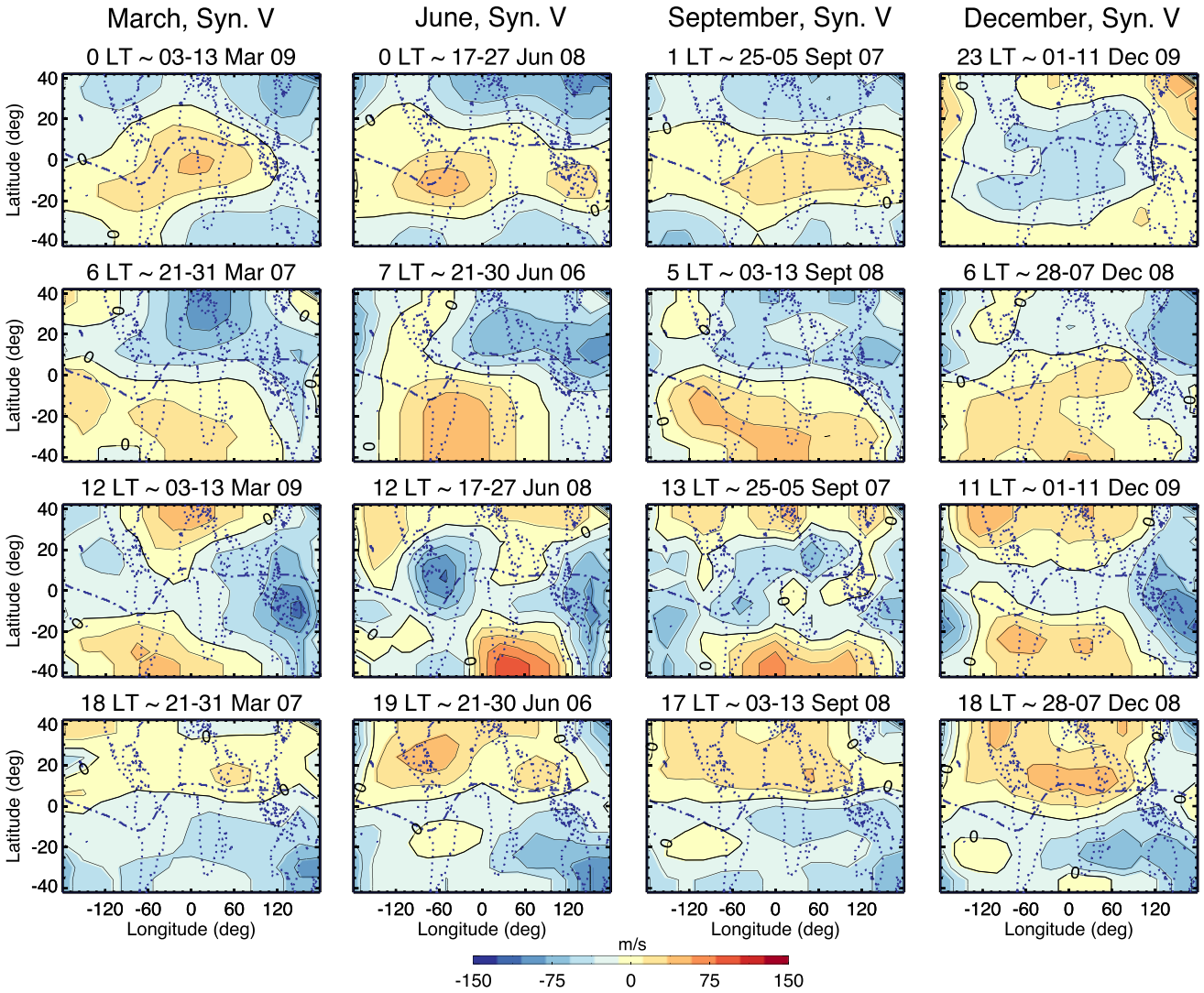

Figure 12. Similar to Figure 11, but for meridional synthetic winds. The seasonal dependency in the meridional winds is not as strong as for the zonal winds. Note the strong longitudinal wave 1 structure and absence of wave 3 and wave 4 structures.

6.6. Seasonal and Local Time Variability of Synthetic Winds

In this section we provide a small sampling of latitude-longitude wind structures obtainable from the CHAMP database to provide a perspective on potential scientific applications not directly addressed in this paper. We begin by demonstrating that both the latitude-longitude variation and magnitude of the winds highly depend on season and local time. Figure 11 shows latitude-longitude structures in synthetic zonal wind for the months of March, June, September, and December at 0 LT, 6 LT, 12 LT, and 18 LT, and give an overview of seasonal and local time dependency of the winds for low solar flux levels and geomagnetic quiet conditions. Note the significant seasonal dependency in the longitudinal structures, with the strong presence of wave 1 in March (0 LT and 12 LT), wave 2 in March (6 LT and 18 LT), September (5 LT, 13 LT, and 17 LT), and December (6 LT, 11 LT, and 23 LT), and wave 4 in September (1 LT and 5 LT). Various tidal perturbations can generate a wave 2 longitude structure in the zonal winds (i.e., DW3, DE1, SW4, S0, and sPW2). *Forbes et al.*'s [2014] findings indicate that SW4 is likely the main contributor to the observed wave 2 structure. This nonmigrating tidal component is also known to maximize around September–March [*Forbes et al.*, 2014], thus explaining the strong wave 2 in March, September, and December. For September at 1 LT (which refers to the 10 day period 25 August to 5 September 2007) we see the clear presence of wave 4 around the equator (i.e., DE3) and at middle low latitudes (i.e., SE2, with greater amplitudes in the Southern Hemisphere, consistent with what is shown in Figure 10). A rather common feature in the seasonal variation is that the average wind velocities

(both eastward and westward) are about 20–30% smaller around December than in other seasons. This is particular evident for 11 LT and 18 LT, with speeds of ±100 m/s in March/June, but limited to ±50–70 m/s in December.

The meridional latitude-longitude wind structures (Figure 12) show significant dependency on local time, similarly to the zonal winds but not much variability with season. For all seasons, at dusk (i.e., 18 LT) the winds tend to be southward in the Southern Hemisphere and northward in the Northern Hemisphere, while this pattern is reversed at dawn (i.e., 6 LT). The midnight meridional winds possess little longitudinal variability, and are mainly northward at low latitude to midlatitude (±25°) for all seasons but December (when they are southward). Note how the absolute speeds of the meridional winds is generally ∼ ±100 m/s. As can also be easily noticed by comparing Figure 12 with Figure 11, the latitude-longitude structures in meridional winds are simpler compared to the zonal winds. The longitudinal structure of the meridional winds (Figure 12) does not possess much wave 3 and wave 4 and is dominated by wave 1 for most seasons and local times. This is similar to what is found by *Clemmons et al.* [2013] in meridional winds derived from Streak ionization gauge measurements. The small wave 3 and wave 4 can be explained by the fact that DE2 and DE3 are quasi-Kelvin waves and thus are known to have substantially smaller meridional winds than zonal winds. From a nearly fixed local time perspective, several tidal perturbations can be responsible for a wave 1 longitude modulation (all the ones with the same $| s - n |$, as discussed in section 6.4): the stationary planetary wave with $s = 1$ (SPW1), the diurnal tide with $s = 0$ (D0), the westward diurnal tide with $s = 2$ (DW2), the semidiurnal westward propagating tide with $s = 1$ (SW1), and $s = 3$ (SW3). We know that SPW1 modulation of DW1 ($n = 1, s = 1$) yields the secondary products D0 ($n = 1, s = 0$) and DW2 ($n = 1, s = 2$), and that SPW1 modulation of SW2 ($n = 2, s = 2$) yields the secondary products SW1 and SW3 [*Forbes et al.*, 2012]. Thus, if the meridional winds have large DW1 and SW2 in the geographic frame, and this structure is tilted into the geomagnetic frame, then we can expect D0, DW2, SW1, and SW3 to be significant components in a geographic frame perspective. A combination of these tidal perturbations due to the effects of the magnetic field is likely to be responsible for the observed wave 1 structure shown in Figure 12. The data in Figures 11 and 12 are provided in the supporting information S1 (ASCII format).

7. Summary and Conclusions

The neutral wind field is a fundamental parameter defining the state and dynamics of the ionosphere-thermosphere system, yet global-scale wind measurements are scarce. Vertical and horizontal winds are responsible for redistributing chemical species and altering the bulk temperature field through adiabatic heating and cooling. Zonal winds are responsible for the generation of electric fields via the *F* region dynamo mechanism, while meridional winds modify the ionosphere by moving plasma up and down magnetic field lines.

CHAMP's slowly precessing orbit provides a unique perspective and different types of insights into the dynamics of the thermosphere than those obtainable from the ground. In this paper, we used neutral and electron densities measured by the CHAMP satellite around 300–350 km to derive pressure gradients and ion drag values. We then solved the horizontal momentum equations of the thermosphere for solar low and geomagnetically quiet conditions to infer zonal and meridional winds. We limited our analyses to midlatitude to low latitude (±45°), where winds driven by convection electric fields are generally negligible. To provide reassurance on the credibility of the derived wind field, we validated our methodology by showing that neutral and electron densities output from NCAR TIME-GCM can be used to derive solutions to the momentum equations that well replicate (with uncertainties up to ∼15%) the winds self-consistently calculated in TIME-GCM. We estimated the total uncertainty in the synthetic winds to be about ±30%, mainly due to errors in the derivation of ion drag (∼ ±14%) and pressure gradient (∼ ±4%) from CHAMP electron and neutral densities. We also compared latitude-longitude synthetic wind structures with CHAMP cross-track winds and found that they share over 65% of the variance, with no detectable bias. We then used synthetic winds to highlight the longitude, latitude, local time, and seasonal variability and presented comparisons with CHAMP cross-track and HWM14 winds in various formats. The main findings from these analyses can be summarized as follows:

1. We found evidence of a strong eastward jet in the postsunset hours around the geomagnetic equator due to decreased ion drag associated with the combined effect of intensified eastward ion drifts due to vertical electric fields and the rapid increase in height of the ionosphere driven by the evening prereversal enhancement of the vertical plasma drift. We also calculated superrotation speeds of 27 m/s at the equator.

2. We found that the HWM14 empirical model largely underestimates (by over ~50%) the latitude, longitude, and local time variability in CHAMP synthetic winds. This is likely due to DE2's poor sampling at solar minimum and the presence of upward propagating tides not captured by the empirical model.
3. We found evidence of vertical wave coupling due to DE3 and SE2, with maximum amplitudes of ~12 m/s in zonal winds (DE3) and ~9 m/s in meridional winds (SE2). Significant asymmetry in the latitudinal variation of DE3 and SE2 are consistent with the presence of higher order modes likely due to the effect of mean winds.
4. We found low-latitude meridional SE2 winds, with amplitudes greater than 8 m/s. These results are supportive of *Oberheide et al.*'s [2011b] and *He et al.*'s [2011] theories that SE2 transequatorial neutral winds are responsible for the antisymmetric component of the ionospheric wave 4.
5. We found strong seasonal and local time dependency in both zonal and meridional winds. Zonal winds show significant latitude-longitude variability for all seasons and local times, whereas meridional winds feature a simpler longitude structure dominated by wave 1. This can be explained as due to the effect of small DE3 meridional winds and the SPW1 modulation of DW1 and SW2 associated with the displacement between geographic and geomagnetic coordinate systems.

Acknowledgments
This work was supported under grant NNX12AD26G from NASA to the University of Colorado under the U.S. Participating Investigator (USPI) Program for the GOCE Mission. CHAMP neutral and electron densities were downloaded from GFZ-Potsdam (isdc.gfz-potsdam.de), while CHAMP neutral winds were provided by the Delft University of Technology (TU Delft). The CHAMP mission was sponsored by the Space Agency of the German Aerospace Center (DLR). The authors would like to thank McArthur Jones Jr. for providing the TIME-GCM simulations used in the validation section of this paper and Jeffrey Thayer and Scott Palo for valuable discussions on vertical viscosity and error analysis.

References

Anderson, D. N., and R. G. Roble (1974), The effect of vertical E × B ionospheric drifts on F region neutral winds in the low-latitude thermosphere, *J. Geophys. Res.*, *79*, 5231–5236, doi:10.1029/JA079i034p05231.

Buonsanto, M. J. (1990), Observed and calculated F_2 peak heights and derived meridional winds at mid-latitudes over a full solar cycle, *J. Atmos. Sol. Terr. Phys.*, *52*, 223–240.

Buonsanto, M. J. (1991), Neutral winds in the thermosphere at mid-latitude over a full solar cycle: A tidal decomposition, *J. Geophys. Res.*, *96*(A3), 3711–3724.

Bruinsma, S. L., and J. M. Forbes (2010a), Large-scale traveling atmospheric disturbances (LSTADs) in the thermosphere inferred from CHAMP, GRACE, and SETA accelerometer data, *J. Atmos. Sol. Terr. Phys.*, *72*(13), 1057–1066, doi:10.1016/j.jastp.2010.06.010.

Bruinsma, S. L., and J. M. Forbes (2010b), Anomalous behavior of the thermosphere during solar minimum observed by CHAMP and GRACE, *J. Geophys. Res.*, *115*, A11323, doi:10.1029/2010JA015605.

Bruinsma, S. L., D. Tamagnan, and R. Biancale (2004), Atmospheric densities derived from CHAMP/STAR accelerometer observations, *Planet. Space Sci.*, *52*, 297–312.

Challinor, R. A. (1969), Neutral air winds in the ionospheric *F*-region for an asymmetric global pressure system, *Planet. Space Sci.*, *18*, 1485–1487.

Chapman, S. (1956), The electrical conductivity of the ionosphere: A review, *Nuovo Cimento*, *4*(4), 1385–1412.

Clemmons, J. H., R. L. Walterscheid, A. B. Christensen, and R. L. Bishop (2013), Rapid, highly structured meridional winds and their modulation by non migrating tides: Measurements from the Streak mission, *J. Geophys. Res. Space Physics*, *118*, 866–877, doi:10.1029/2012JA017661.

Coley, W. R., R. A. Heelis, and N. W. Spencer (1994), Comparison of low- latitude ion and neutral zonal drift using DE2 data, *J. Geophys. Res.*, *99*, 341–348.

Cooke, D. L., W. Turnbull, C. Roth, A. Morgan, and R. Redus (2003), Ion drift-meter status and calibration, in *First Champ Mission Results for Gravity, Magnetic, and Atmospheric Studies*, edited by C. Reigber, H. Lühr, and P. Schwintzer, pp. 212–219, Springer, New York.

Deng, Y., G. Lu, Y.-S. Kwak, E. Sutton, J. Forbes, and S. Solomon (2009), Reversed ionospheric convections during the November 2004 storm: Impact on the upper atmosphere, *J. Geophys. Res.*, *114*, A07313, doi:10.1029/2008JA013793.

Dickinson, R. E., E. C. Ridley, and R. G. Roble (1981), A three-dimensional general circulation model of the thermosphere, *J. Geophys. Res.*, *86*, 1499–1512.

Doornbos, E. (2011), Thermospheric density and wind determination from satellite dynamics, PhD thesis, TU Delft, Netherlands.

Doornbos, E., J. van den Ijssel, H. Lühr, M. Förster, and G. Koppenwallner (2010), Neutral density and crosswind determination from arbitrarily oriented multi-axis accelerometers on satellites, *J. Spacecr. Rockets*, *47*, 580–589, doi:10.2514/1.48114.

Drob, D. P., et al. (2015), An update to the Horizontal Wind Model (HWM): The quiet time thermosphere, *Earth Space Sci.*, *2*, 301–319, doi:10.1002/2014EA000089.

England, S. L., T. J. Immel, E. Sagawa, S. B. Henderson, M. E. Hagan, S. B. Mende, H. U. Frey, C. M. Swenson, and L. J. Paxton (2006), Effect of atmospheric tides on the morphology of the quiet time, postsunset equatorial ionospheric anomaly, *J. Geophys. Res.*, *111*, A10S19, doi:10.1029/2006JA011795.

Forbes, J. M., and H. B. Garrett (1979), Theoretical studies of atmospheric tides, *Rev. Geophys.*, *17*(8), 1951–1981, doi:10.1029/RG017i008p01951.

Forbes, J. M., M. Codrescu, and T. J. Hall (1988), On the utilization of ionosonde data to analyze the latitudinal penetration of ionospheric storm effects, *Geophys. Res. Lett.*, *15*, 249–252.

Forbes, J. M., S. L. Bruinsma, Y. Miyoshi, and H. Fujiwara (2008), A solar terminator wave in thermosphere neutral densities measured by the CHAMP satellite, *Geophys. Res. Lett.*, *35*, L14802, doi:10.1029/2008GL034075.

Forbes, J. M., S. L. Bruinsma, X. Zhang, and J. Oberheide (2009), Surface-exosphere coupling due to thermal tides, *Geophys. Res. Lett.*, *36*, L15812, doi:10.1029/2009GL038748.

Forbes, J. M., X. Zhang, and S. Bruinsma (2012), Middle and upper thermosphere density structures due to nonmigrating tides, *J. Geophys. Res.*, *117*, A11306, doi:10.1029/2012JA018087.

Forbes, J. M., X. Zhang, S. Bruinsma, and J. Oberheide (2013), Lunar semidiurnal tide in the thermosphere under solar minimum condition, *J. Geophys. Res. Space Physics*, *118*, 1788–1801, doi:10.1029/2012JA017962.

Forbes, J. M., X. Zhang, and S. L. Bruinsma (2014), New perspectives on thermosphere tides—2. Penetration to the upper thermosphere, *Earth Planets Space*, *66*, 122, doi:10.1186/1880-5981-66-122.

Förster, M., S. Rentz, W. Köhler, H. Liu, and S. E. Haaland (2008), IMF dependence of high-latitude thermospheric wind pattern derived from CHAMP cross-track measurements, *Ann. Geophys.*, *26*, 1581–1595.

Fuller-Rowell, T. J., M. V. Codrescu, B. G. Fejer, W. Borer, F. Marcos, and D. N. Anderson (1997), Dynamics of the low-latitude thermosphere: Quiet and disturbed conditions, *J. Atmos. Sol. Terr. Phys.*, *59*, 1533–1540, doi:10.1016/S1364-6826(96)00154-X.

Gasperini, F., J. M. Forbes, E. N. Doornbos, and S. L. Bruinsma (2015), Wave coupling between the lower and middle thermosphere as viewed from TIMED and GOCE, *J. Geophys. Res. Space Physics*, *120*, 5788–5804, doi:10.1002/2015JA021300.

Geisler, J. E. (1966), Atmospheric winds in the middle latitude *F*-region, *J. Atmos. Sol. Terr. Phys.*, *28*(8), 703–720, doi:10.1016/0021-9169(66)90020-1.

Geisler, J. E. (1967), A numerical study of the wind system in the middle thermosphere, *J. Atmos. Sol. Terr. Phys.*, *29*(12), 1469–1482, doi:10.1016/0021-9169(67)90100-6.

Guo, J., W. Wan, J. M. Forbes, E. Sutton, R. S. Nerem, and S. Bruinsma (2008), Interannual and latitudinal variability of the thermosphere density annual harmonics, *J. Geophys. Res.*, *113*, A08301, doi:10.1029/2008JA013056.

Hagan, M. E., and J. M. Forbes (2002), Migrating and nonmigrating diurnal tides in the middle and upper atmosphere excited by tropospheric latent heat release, *J. Geophys. Res.*, *107*(D24), 4754, doi:10.1029/2001JD001236.

Hagan, M. E., J. L. Chang, and S. K. Avery (1997), GSWM estimates of non-migrating tidal effects, *J. Geophys. Res.*, *102*(16), 439–452, doi:10.1029/97JD01269.

Häusler, K., and H. Lühr (2009), Nonmigrating tidal signals in the upper thermospheric zonal wind at equatorial latitudes as observed by CHAMP, *Ann. Geophys.*, *27*, 2643–2652.

Häusler, K., H. Lühr, S. Rentz, and W. Köhler (2007), A statistical analysis of longitudinal dependences of upper thermospheric zonal winds at dip equator latitudes derived from CHAMP, *J. Atmos. Sol. Terr. Phys.*, *69*, 1419–1430.

He, M., L. Liu, W. Wan, and Y. Wei (2011), Strong evidence for couplings between the ionospheric wave-4 structure and atmospheric tides, *Geophys. Res. Lett.*, *38*, L14101, doi:10.1029/2011GL047855.

Hedin, A. E. (1991), Extension of the MSIS thermospheric model into the middle and lower atmosphere, *J. Geophys. Res.*, *96*(A2), 1159–1172.

Immel, T. J., E. Sagawa, S. L. England, S. B. Henderson, M. E. Hagan, S. B. Mende, H. U. Frey, C. M. Swenson, and L. J. Paxton (2006), Control of equatorial ionospheric morphology by atmospheric tides, *Geophys. Res. Lett.*, *33*, L15108, doi:10.1029/2006GL026161.

Jacchia, L. G. (1971), Revised static models of the thermosphere and exosphere with empirical temperature profiles, *Smithson. Astrophys. Obs. Spec. Rep. 332*, SAO, Cambridge, Mass.

Jacchia, L. G., and J. Slowey (1964), Temperature variations in the upper atmosphere during geomagnetically quiet intervals, *J. Geophys. Res.*, *69*(19), 4145–4148, doi:10.1029/JZ069i019p04145.

Jones, M., Jr., J. M. Forbes, M. E. Hagan, and A. Maute (2013), Non-migrating tides in the ionosphere-thermosphere: In situ versus tropospheric sources, *J. Geophys. Res. Space Physics*, *118*, 2438–2451, doi:10.1002/jgra.50257.

Jones, M., Jr., J. M. Forbes, M. E. Hagan, and A. Maute (2014), Impacts of vertically propagating tides on the mean state of the ionosphere-thermosphere system, *J. Geophys. Res. Space Physics*, *119*, 2197–2213, doi:10.1002/2013JA019744.

Killeen, T. L., and R. G. Roble (1984), An analysis of the high-latitude thermospheric wind pattern calculated by a thermospheric General Circulation Model: 1. Momentum forcing, *J. Geophys. Res.*, *89*(A9), 7509–7522, doi:10.1029/JA089iA09p07509.

King-Hele, D. G. (1964), The rotational speed of the upper atmosphere determined from changes in satellite orbits, *Planet. Space Sci.*, *12*, 835–853.

King-Hele, D. G., and D. M. C. Walker (1983), Upper-atmosphere zonal winds from satellite orbit analysis, *Planet. Space Sci.*, *31*, 509–535.

Kwak, Y.-S., A. D. Richmond, Y. Deng, J. M. Forbes, and K.-H. Kim (2009), Dependence of the high-latitude thermospheric densities on the interplanetary magnetic field, *J. Geophys. Res.*, *114*, A05304, doi:10.1029/2008JA013882.

Kwak, Y.-S., K.-H. Kim, Y. Deng, and J. M. Forbes (2011), Response of thermosphere density to changes in interplanetary magnetic field sector polarity, *J. Geophys. Res.*, *116*, A11316, doi:10.1029/2011JA016938.

Knipp, D., L. Kilcommons, L. Hunt, M. Mlynczak, V. Pilipenko, B. Bowman, Y. Deng, and K. Drake (2013), Thermospheric damping response to sheath-enhanced geospace storms, *Geophys. Res. Lett.*, *40*, 1263–1267, doi:10.1002/grl.50197.

Lei, J., J. P. Thayer, J. M. Forbes, E. K. Sutton, R. S. Nerem, M. Temmer, and A. M. Veronig (2008), Global thermospheric density variations caused by high-speed solar wind streams during the declining phase of solar cycle 23, *J. Geophys. Res.*, *113*, A11303, doi:10.1029/2008JA013433.

Lei, J., J. P. Thayer, and J. M. Forbes (2010), Longitudinal and geomagnetic activity modulation of the equatorial thermosphere anomaly, *J. Geophys. Res.*, *115*, A08311, doi:10.1029/2009JA015177.

Lei, J., J. P. Thayer, W. Wang, and R. L. McPherron (2011), Impact of CIR storms on thermosphere density variability during the solar minimum of 2008, *Sol. Phys.*, *274*(1), 427–437, doi:10.1007/s11207-010-9563-y.

Lieberman, R. S., R. A. Akmaev, T. J. Fuller-Rowell, and E. Doornbos (2013), Thermospheric zonal mean winds and tides revealed by CHAMP, *Geophys. Res. Lett.*, *40*, 2439–2443, doi:10.1002/grl.50481.

Lin, C. H., W. Wang, M. E. Hagan, C. C. Hsiao, T. J. Immel, M. L. Hsu, J. Y. Liu, L. J. Paxton, T. W. Fang, and C. H. Liu (2007), Plausible effect of atmospheric tides on the equatorial ionosphere observed by the FORMOSAT-3/COSMIC: Three-dimensional electron density structures, *Geophys. Res. Lett.*, *34*, L11112, doi:10.1029/2007GL029265.

Lindzen, R. S., S. S. Hong, and J. M. Forbes (1977), Semidiurnal Hough mode extensions in the thermosphere and their application, *Memo. Rep. 3442*, Nav. Res. Lab., Washington, D. C.

Liu, H., and H. Lühr (2005), Strong disturbance of the upper thermospheric density due to magnetic storms: CHAMP observations, *J. Geophys. Res.*, *110*, A09S29, doi:10.1029/2004JA010908.

Liu, H., and S. Watanabe (2008), Seasonal variation of the longitudinal structure of the equatorial ionosphere: Does it reflect tidal influences from below?, *J. Geophys. Res.*, *113*, A08315, doi:10.1029/2008JA013027.

Liu, H., H. Lühr, S. Watanabe, W. Köhler, V. Henize, and P. Visser (2006), Zonal winds in the equatorial upper thermosphere: Decomposing the solar flux, geomagnetic activity, and seasonal dependencies, *J. Geophys. Res.*, *111*, A07307, doi:10.1029/2005JA011415.

Liu, H., H. Lühr, and S. Watanabe (2007), Climatology of the equatorial thermospheric mass density anomaly, *J. Geophys. Res.*, *112*, A05305, doi:10.1029/2006JA012199.

Liu, H., H. Lühr, and S. Watanabe (2009), A solar terminator wave in thermospheric wind and density simultaneously observed by CHAMP, *Geophys. Res. Lett.*, *36*, L10109, doi:10.1029/2009GL038165.

Liu, L., X. Luan, W. Wan, J. Lei, and B. Ning (2003), Seasonal behavior of equivalent winds over Wuhan derived from ionospheric data in 2000 - 2001, *Adv. Space Res.*, *32*, 1765–1770.

Liu, L., X. Luan, W. Wan, J. Lei, and B. Ning (2004), Solar activity variations of equivalent winds derived from global ionosonde data, *J. Geophys. Res.*, *109*, A12305, doi:10.1029/2004JA010574.

Lomidze, L., and L. Scherliess (2015), Estimation of thermospheric zonal and meridional winds using a Kalman filter technique, *Space Weather*, *13*, 747–760, doi:10.1002/2015SW001250.

Lomidze, L., L. Scherliess, and R. W. Schunk (2015), Magnetic meridional winds in the thermosphere obtained from Global Assimilation of Ionospheric Measurements (GAIM) model, *J. Geophys. Res. Space Physics*, *120*, 8025–8044, doi:10.1002/2015JA021098.
Luan, X., and S. C. Solomon (2008), Meridional winds derived from COSMIC radio occultation measurements, *J. Geophys. Res.*, *113*, A08302, doi:10.1029/2008JA013089.
Lühr, H., M. Rother, W. Köhler, P. Ritter, and L. Grunwaldt (2004), Thermospheric up-welling in the cusp region: Evidence from CHAMP observations, *Geophys. Res. Lett.*, *31*, L06805, doi:10.1029/2003GL019314.
Lühr, H., S. Rents, P. Ritter, H. Liu, and K. Häusler (2007a), Average thermospheric wind pattern over the polar regions, as observed by CHAMP, *Ann. Geophys.*, *25*, 1093–1101.
Lühr, H., K. Häusler, and C. Stolle (2007b), Longitudinal variation of F region electron density and thermospheric zonal wind caused by atmospheric tides, *Geophys. Res. Lett.*, *34*, L16102, doi:10.1029/2007GL030639.
McNamara, L. F., D. L. Cooke, C. E. Valladares, and B. W. Reinisch (2007), Comparison of CHAMP and digisonde plasma frequencies at Jicamarca, Peru, *Radio Sci.*, *42*, RS2005, doi:10.1029/2006RS003491.
Meriwether, J. W. (2006), Studies of thermospheric dynamics with a Fabry-Perot interferometer network: A review, *J. Atmos. Sol. Terr. Phys.*, *68*(13), 1576–1589, doi:10.1016/j.jastp.2005.11.014.
Miyoshi, Y., H. Fujiwara, H. Jin, H. Shinagawa, and H. Liu (2012), Numerical simulation of the equatorial wind jet in the thermosphere, *J. Geophys. Res.*, *117*, A03309, doi:10.1029/2011JA017373.
Oberheide, J., J. M. Forbes, K. Häusler, Q. Wu, and S. L. Bruinsma (2009), Tropospheric tides from 80 to 400 km: Propagation, interannual variability, and solar cycle effects, *J. Geophys. Res.*, *114*, D00I05, doi:10.1029/2009JD012388.
Oberheide, J., J. M. Forbes, X. Zhang, and S. L. Bruinsma (2011a), Climatology of upward propagating diurnal and semidiurnal tides in the thermosphere, *J. Geophys. Res.*, *116*, A11306, doi:10.1029/2011JA016784.
Oberheide, J., J. M. Forbes, X. Zhang, and S. L. Bruinsma (2011b), Wave-driven variability in the ionosphere-thermosphere-mesosphere system from TIMED observations: What contributes to the wave 4?, *J. Geophys. Res.*, *116*, A01306, doi:10.1029/2010JA015911.
Pedatella, N. M., J. M. Forbes, and J. Oberheide (2008), Intra-annual variability of the low-latitude ionosphere due to nonmigrating tides, *Geophys. Res. Lett.*, *35*, L18104, doi:10.1029/2008GL035332.
Richmond, A. D. (1971), Tidal winds at ionospheric heights, *Radio Sci.*, *6*, 175–189.
Richmond, A. D., E. C. Ridely, and R. G. Roble (1992), A thermosphere/ionosphere general circulation model with coupled electrodynamics, *Geophys. Res. Lett.*, *19*, 601–604.
Rishbeth, H. (1967), The effect of winds on the ionospheric F_2-peak, *J. Atmos. Sol. Terr. Phys.*, *29*, 225–238.
Rishbeth, H. (1971), The *F*-layer dynamo, *Planet. Space Sci.*, *19*, 263–267.
Rishbeth, H. (2000), The equatorial *F*-layer: Progress and puzzles, *Ann. Geophys.*, *18*(7), 730–739, doi:10.1007/s00585-000-0730-6.
Rishbeth, H. (2002), Whatever happened to superrotation, *J. Atmos. Sol. Terr. Phys.*, *64*, 1351–1360.
Rishbeth, H., and O. K. Garriott (1969), *Introduction to Ionospheric Physics*, p. 331, Academic, New York.
Rishbeth, H., S. Ganguly, and J. C. G. Walker (1978), Field-aligned and field-perpendicular velocities in the ionospheric F_2 layer, *J. Atmos. Sol. Terr. Phys.*, *40*, 767–784.
Roble, R. G., and E. C. Ridley (1994), A Thermosphere-Ionosphere-Mesosphere-Electrodynamics General Circulation Model (TIME-GCM): Equinox solar cycle minimum simulations (30–500 km), *Geophys. Res. Lett.*, *21*, 417–420.
Roble, R. G., E. C. Ridely, A. D. Richmond, and R. E. Dickinson (1988), A coupled thermosphere/ionosphere general circulation model, *Geophys. Res. Lett.*, *15*, 1325–1328.
Sagawa, E., T. J. Immel, H. U. Frey, and S. B. Mende (2005), Longitudinal structure of the equatorial anomaly in the nighttime ionosphere observed by IMAGE/FUV, *J. Geophys. Res.*, *110*, A11302, doi:10.1029/2004JA010848.
Salah, J. E., and J. M. Holt (1974), Midlatitude thermospheric winds from incoherent scatter radar and theory, *Radio Sci.*, *9*(2), 301–313, doi:10.1029/RS009i002p00301.
Sutton, E. K., J. M. Forbes, and R. S. Nerem (2005), Global thermospheric neutral density and wind response to the severe 2003 geomagnetic storms from CHAMP accelerometer data, *J. Geophys. Res.*, *110*, A09S40, doi:10.1029/2004JA010985.
Talaat, E. R., and R. S. Lieberman (2010), Direct observations of nonmigrating diurnal tides in the equatorial thermosphere, *Geophys. Res. Lett.*, *37*, L04803, doi:10.1029/2009GL041845.
Thayer, J. P., J. Lei, J. M. Forbes, E. K. Sutton, and R. S. Nerem (2008), Thermospheric density oscillations due to periodic solar wind high-speed streams, *J. Geophys. Res.*, *113*, A06307, doi:10.1029/2008JA013190.
Truskowski, A. O., J. M. Forbes, X. Zhang, and S. E. Palo (2014), New perspectives on thermosphere tides—1. Lower thermosphere spectra and seasonal-latitudinal structures, *Earth Planets Space*, *66*, 136, doi:10.1186/s40623-014-0136-4.
Walterscheid, R. L., and G. Crowley (2015), Thermal cell structures in the high-latitude thermosphere induced by ion drag, *J. Geophys. Res. Space Physics*, *120*, 6837–6850, doi:10.1002/2015JA021122.
Wharton, L. E., N. W. Spencer, and H. G. Mayr (1984), The Earth's thermospheric superrotation from Dynamics Explorer 2, *Geophys. Res. Lett.*, *11*, 531–533.
Zhang, X., J. M. Forbes, and M. E. Hagan (2010a), Longitudinal variation of tides in the MLT region: 1. Tides driven by tropospheric net radiative heating, *J. Geophys. Res.*, *115*, A06316, doi:10.1029/2009JA014897.
Zhang, X., J. M. Forbes, and M. E. Hagan (2010b), Longitudinal variation of tides in the MLT region: 2. Relative effects of solar radiative and latent heating, *J. Geophys. Res.*, *115*, A06317, doi:10.1029/2009JA014898.